

Transition from Capacitive to Inductive Hysteresis: A Neuron-Style Model to Correlate I – V Curves to Impedances of Metal Halide Perovskites

Cedric Gonzales, Antonio Guerrero,* and Juan Bisquert*



Cite This: *J. Phys. Chem. C* 2022, 126, 13560–13578



Read Online

ACCESS |

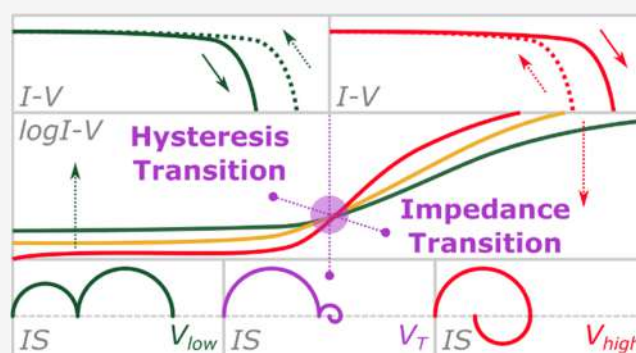
Metrics & More

Article Recommendations

Supporting Information

ABSTRACT: Metal halide perovskite (MHP) devices often show different types of hysteresis in separate voltage domains. At low voltage, the impedance response is capacitive, and the cell gives regular hysteresis. At high voltage, the hysteresis is inverted, corresponding to an inductive response that causes a negative capacitance feature. We calculate the hysteresis current due to a chemical inductor model, and we show that the current is inversely proportional to the voltage scan rate. We formulate a general dynamical model for the solar cell response in the style of neuronal models for the action potential, based on a few differential equations. The model allows us to track the transition from capacitive to inductive properties, both by impedance spectroscopy and current–voltage measurements at different voltage sweep rates.

We obtain a correlation of the time constants for the capacitor and the inductor. We interpret the origin of the low-frequency features in terms of ion-controlled surface recombination. This explains the strong correlation of the low-frequency capacitance and inductor, as both originate from the same mechanism. The methodology derived in this paper provides great control over the dynamic properties of metal halide perovskite solar cells, even in cases in which there are qualitative changes of the solar cell current–voltage response over a broad voltage range.



1. INTRODUCTION

Metal halide perovskites (MHP) have established a new photovoltaic (PV) technology for large solar energy conversion efficiencies with low-cost, solution-processed materials.^{1–4} The MHP can be described as ABX_3 where A = monovalent cations (i.e., methyl ammonium, MA; formamidinium, FA), B = divalent cations (i.e., Pb^{2+}), and X = halide anions (i.e., I^-). It is possible to use combinations of cations (MA, FA, Cs, and Rb) and anions (I, Br) to modify the band gap, efficiency, and stability for different types of applications.^{5–8} For example, $MAPbBr_3$ forms a semiconductor with a wide band gap (2.3 eV) useful for tandem solar cells in combination with Si.^{9,10} In addition, the external interfaces play a very important role, and improvement of the charge extraction layers has enhanced the charge external collection and stability of the devices.^{11,12}

MHP semiconductors show mixed ionic–electronic conduction in which a significant ionic conductivity exists in addition to the electronic photoconductivity.^{13–16} These effects cause intrinsic memory effects (hysteresis) in current–voltage (I – V)^{17–26} that lead to substantial differences in the forward and reverse scan currents and permanent resistive changes. By different empirical methods, it has been possible to minimize hysteresis effects in perovskite solar cells.^{27–29} However, hysteresis persists in recent high-performance configurations,

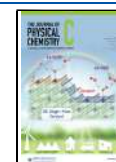
such as tandem solar cells.^{30–33} In addition, hysteresis and memory effects allow the storage of information by modification of device conductivity. This can be exploited in memristors^{34–36} and artificial synapse devices^{37,38} in which MHPs are used for nonoptoelectronic applications related to memory storage and neuromorphic computation.^{39–41}

Impedance spectroscopy (IS) consists of the electrical measurement of the device at a steady-state potential V by a small perturbation of current-to-voltage at varying angular frequency ω . It is a central technique for the characterization of PV cells and electrochemical devices.^{42,43} The knowledge about the system properties is represented by an equivalent circuit (EC), in which elements change according to external conditions. Extensive studies of IS of MHP^{44–50} have provided a basic picture of the shape of spectra and EC models. These results show that the IS description of an MHP measured over a broad voltage range undergoes transformations in which some

Received: April 20, 2022

Revised: July 23, 2022

Published: August 4, 2022



elements appear and dominate the impedance spectra while others lose relevance. There is a variety of reasons for this, such as that elements show an exponential dependence on bias voltage, causing large changes of their values. Another one is that elements may be truly activated at some voltage, as observed in the onset of a large current in memristors.^{36,51}

It has been remarked that hysteresis and impedance are closely related properties since frequency and time domain response are intimately connected.^{25,52} However, a quantitative analysis of this assertion in complex cases has not been presented before. This paper uses different tools that have been derived in recent years to provide a more complete methodology that addresses intricate changes of hysteresis and impedance response often found in perovskite solar cells. We aim to make a modelistic description of I – V curves that change at different scan rates, compatible with the impedance spectroscopy properties.

There are different studies on this problem based on drift-diffusion simulations and related approaches.^{53–61} Here, we introduce a different complementary approach, in which the model is formed by a small number of equations that can describe consistently the different techniques: the I – V curves at different scan rates and other large perturbation methods such as the response to large voltage or illumination steps,⁶² in the one hand, and in the other hand, the small perturbation measurements like IS, IMPS, and IMVS.⁵² Such a model provides an outstanding tool to correlate the different measurements and to make predictions of solar cell characteristics based on a few fast measurement characterizations.

In particular, the model should have the following goals.

- (1) Explain the tendencies of hysteresis in current–voltage and impedance spectroscopy with a single unified model that contains only a few number of parameters that account for the dominant properties of the device.
- (2) Identify and explain correlations of the impedance parameters.
- (3) Explain why the inductive behavior (negative capacitance) appears at high voltage in halide perovskite solar cells.
- (4) Explain why it is observed in some cells and not in others.

We use as inspiration the models of neuron theory that describe extraordinarily complex phenomena including spiking, bifurcation, and potentiation with just a few nonlinear differential equations (a total number from 2 to 4).^{63–65} Recently, these models for the time domain responses have been put into correspondence with the impedance spectroscopy properties.^{66,67} The same methodology has been applied to halide perovskite memristors.^{51,68}

Here, we address the much broader problem of hysteresis and impedance properties of halide perovskite solar cells. We show the general properties of the transformation of EC elements along the voltage changes in MHP solar cells. To summarize the available knowledge and tools, we present in the next section a summary of the properties of hysteresis. Then, we show the experimental results. Methylammonium lead bromide (MAPbBr₃) solar cells are selected as they present a manifest transformation from the capacitive response at low voltage to a large inductor feature at high voltage.⁶⁹ The study in the dark conditions produces highly controlled conditions as compared to under illumination, which facilitates model validation. Furthermore, it avoids the photoinduced effects with the increased ionic conductivity and photodegradation. Then, we

build the model to explain quantitatively the changing properties of hysteresis in relation to the variation of EC properties. We track the evolution of parameters, and we find unexpected links between them. We provide a physical interpretation and finish with some conclusions.

2. CAPACITIVE AND INDUCTIVE HYSTERESIS IN HALIDE PEROVSKITES

2.1. Hysteresis and Stability. Hysteresis is obtained when measuring the current of the solar cell under a voltage sweep at a constant velocity. The I – V curves become separated in the forward and reverse, as shown in Figure 1a,b. Hysteresis of current–voltage is a transient effect.^{17–24} By waiting for a sufficiently long time, the current can be stabilized, and methods are proposed to establish the power conversion efficiency independent of hysteresis effects.^{70–73} But in a reasonable dynamic measurement, a divergence is often found between forward and reverse curves. It happens when the internal

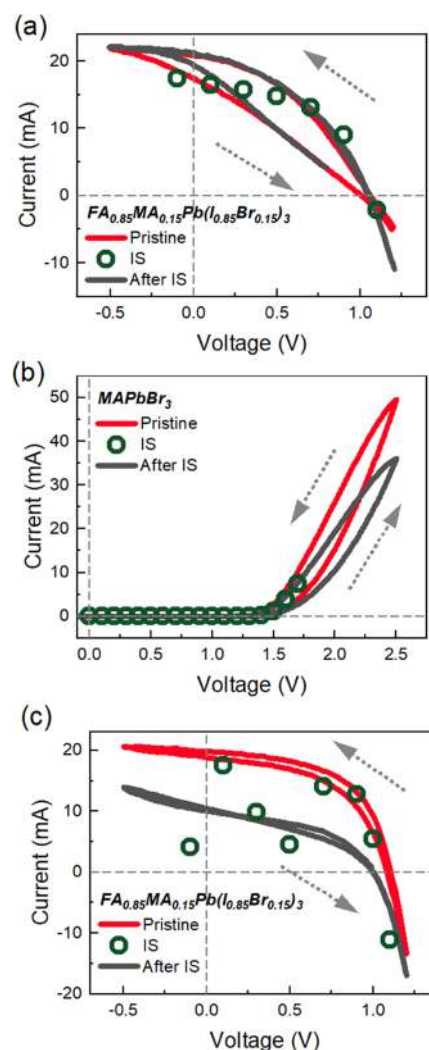


Figure 1. Representative I – V response of halide perovskite solar cells measured at 50 mV/s, showing the pristine as-prepared device and after IS measurements. (a) Mixed halide perovskite solar cells under illumination. (b) MAPbBr₃ in the dark. (c) Mixed halide perovskite solar cells under illumination. The current extracted during the IS measurement is shown in circles to determine the correspondence of the electrical measurements J – V and IS.

dynamic timescales of the device intersect the time duration of the measurement. Note that the forward photocurrent is smaller in Figure 1a than the reverse current (normal hysteresis) and conversely in Figure 1b (inverted hysteresis).

It is well known that one has to be cautious in MHP characterization. There are many types of transient phenomena in halide perovskites. These effects may be caused by the sample being away from equilibrium at the beginning of the measurement or when a fresh sample is aiming at operation stability.⁷⁴ One example is the famous “pretreatment effect”, in which one can produce favorable or deleterious effects according to initial biasing.⁷⁵ Pockett et al. showed that rapidly changing initial features of a carbon-based perovskite solar cell are captured consistently by TPV and IMVS techniques.⁷⁶ An example of a solar cell that is changing its characteristics by voltage cycling in the dark is shown in Figure 1b and under illumination in Figure 1a,c. These properties have been attributed to the slow ion transit effects that create uncompensated electrical fields or modify the interfaces by surface polarization effects.^{61,77}

Figure 1a shows a robust and reproducible solar cell where current–voltage under voltage sweep and the current measured during IS measurement agree. In this paper, we are interested in an initial situation that has been stabilized so that the results of small or large perturbation measurements can be associated entirely with the applied signal and not with hidden memory effects or sample drift effects. Based on this assumption, we can attribute an EC response to different equilibrated stages of the dynamics, and the full evolution in a voltage excursion can be reasonably treated by parameters that depend on the voltage.

2.2. Capacitive Hysteresis. The first well-identified hysteresis effect in halide perovskite was the description of capacitive current by Garcia-Belmonte and co-workers, see Figure 2 that shows the results associated with the low-frequency capacitance of halide perovskites.⁷⁸ Capacitive current effects are very common in electrochemical devices.^{79,80} Capacitive hysteresis for diodes in the dark occurs with a forward current that is larger than the reverse current, as shown in Figure 2a,b. The capacitive current is proportional to the scan rate, Figure 2c, and it changes sign when inverting the scan direction, producing the characteristic square shape of Figure 2d. Capacitive hysteresis was often observed in other types of devices such as dye-sensitized solar cells.⁸¹

Figure 3 shows the correlation of the low-frequency capacitance with the amount of hysteresis in MHP solar cells with different types of contacts.²¹ The huge hysteresis response in Figure 3a is due to the large capacitive effect of TiO₂ contact, shown in Figure 3d,e. In contrast, for the inverted structure, the I – V hysteresis and the equilibration time are decreased, Figure 3b,c. In the I – V illuminated characteristic of the solar cell in Figure 3a, the increasing recombination current at large voltage turns more negative, hence in this representation of capacitive hysteresis, the forward current becomes smaller than the reverse current.

For the modeling of capacitive hysteresis, we use the following equation

$$I_{\text{tot}} = C_m \frac{dV}{dt} + I_b(V) \quad (1)$$

Here, I_{tot} is the total current, V is the voltage across the device, C_m is the capacitance, and I_b is a conduction current that may have different types of values. For an ohmic current with a constant resistance R_b , we have

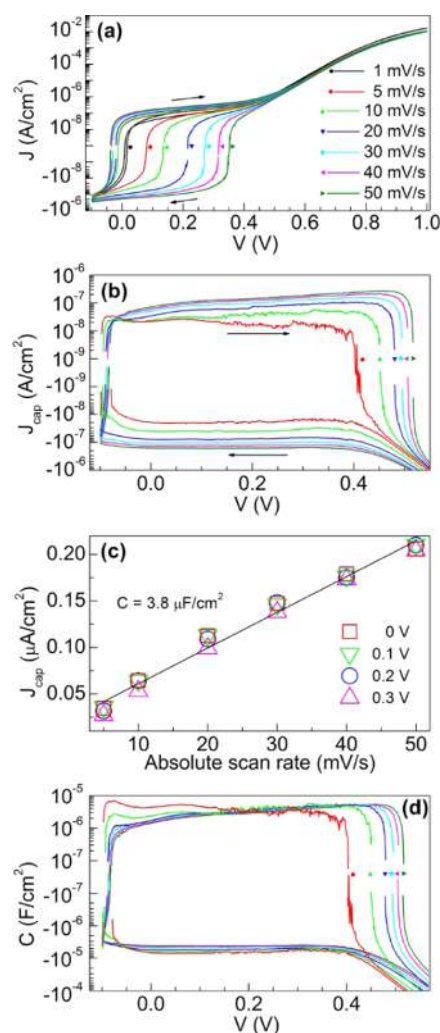


Figure 2. Measurements of CH₃NH₃PbI₃ solar cell in the dark. (a) J – V curves at different scan rates as indicated with logarithmic scaled currents. (b) Capacitive current density J_{cap} extracted from J – V curves. (c) Current proportional to the scan rate at different applied voltages. (d) Capacitance calculated from J_{cap} , s^{−1} at different scan rates as in panel (a). Reproduced from ref 78. Copyright 2015 American Chemical Society.

$$I_b(V) = \frac{V}{R_b} \quad (2)$$

For a recombination current in a solar cell diode at forward bias

$$I_b(V) = I_{b0} e^{qV/m_b k_B T} \quad (3)$$

Here, I_{b0} is a constant prefactor, q is the elementary charge, k_B is the Boltzmann’s constant, T is the absolute temperature, and m_b is an ideality factor.^{82–84} For practical reasons, we define the ideality factor with dimension of voltage

$$V_b = \frac{m_b k_B T}{q} \quad (4)$$

Then eq 3 can be expressed

$$I_b(V) = I_{b0} e^{V/V_b} \quad (5)$$

For a voltage sweep measurement at velocity v_v , we have

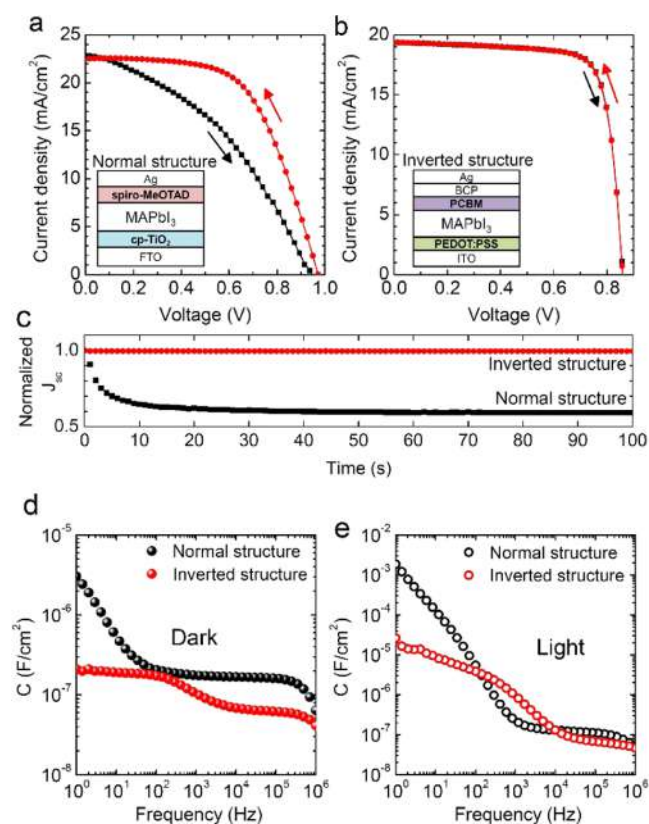


Figure 3. (a) J - V hysteresis of the cp-TiO₂/MAPbI₃/spiro-MeOTAD (normal) structure and (b) the PEDOT:PSS/MAPbI₃/PCBM (inverted) structure. During the J - V scan, the current was acquired for 100 ms after applying a given voltage. (c) Normalized time-dependent short-circuit current density (J_{sc}) of the normal and the inverted structures. Open-circuit condition under one sun illumination was maintained before measuring J_{sc} . Capacitance–frequency (C - F) curves (d) under dark and (e) one sun illumination at short-circuit condition (bias voltage = 0 V). Reproduced from ref 21. Copyright 2015 American Chemical Society.

$$V = V_0 + v_r t \quad (6)$$

Then eq 1 becomes

$$I_{tot}(V) = C_m v_r + I_{b0} e^{V/V_b} \quad (7)$$

The capacitive current is proportional to the scan rate, as commented earlier. In a forward scan, the capacitive current is added to the diode exponential curve while subtracted in the reverse scan (negative v_r). This is the feature of capacitive hysteresis. The representation of eq 7 is shown in Figure 4a,b. The properties of the current describe very well those reported in Figure 2.

2.3. Capacitive Impedance. In the impedance spectroscopy measurement, we use a sinusoidal small perturbation $\hat{V}(t)$ over a steady-state \bar{V} , $V = \bar{V} + \hat{V}(t)$. For the small perturbation components, eq 1 becomes

$$\hat{I}_{tot} = C_m \frac{d\hat{V}}{dt} + \frac{1}{R_{rec}} \hat{V} \quad (8)$$

where the recombination resistance is, by eq 3

$$R_{rec} = \left(\frac{\partial I_b}{\partial V} \right)^{-1} = \frac{V_b}{I_{b0}} e^{-V/V_b} \quad (9)$$

Taking the Laplace transformation of eq 8, we obtain

$$\hat{I}_{tot} = \left(C_m i\omega + \frac{1}{R_{rec}} \right) \hat{V} \quad (10)$$

Therefore the impedance is

$$Z = \frac{\hat{V}}{\hat{I}_{tot}} = \left(C_m i\omega + \frac{1}{R_{rec}} \right)^{-1} \quad (11)$$

This last result is a parallel RC connection EC, Figure 4c, that forms a semiarc in the complex impedance plot, Figure 4d. The associated time constant is $\tau_m = R_{rec} C_m$. The elementary EC of a solar cell^{43,85} has the same structure as eq 11, but C_m is interpreted as a chemical capacitance that depends exponentially on the potential.⁸⁶

The characteristic impedance patterns of halide perovskites have been recently summarized.⁴³ The simplest behavior found experimentally is given by two arcs as shown in Figure 5b and the related capacitance step in the frequency plot of Figure 5c. It is described by an EC formed by two resistances and two capacitors, Figure 5a. We denote the low-frequency arc resistance as R_1 and the high-frequency arc resistance as R_3 .⁸⁷ The meaning of the resistances depends on the illumination conditions, but the low-frequency arc usually relates to the perovskite/contacts interface (ion migration, accumulation, and recombination).⁸⁸ Hence, the capacitance C_1 is a surface capacitance related to ionic–electronic phenomena, and C_g is a dielectric geometrical capacitance. The parallel connection of R_1 to C_1 generates the low-frequency arc. Typical experimental parameters as a function voltage are shown in Figure 6.

It should be noted that Figure 5a cannot be obtained with a simple extension of eq 1. At least two voltages in series need to be used.²⁵ Such generalization will be described below.

Figure 6 shows characteristic results of the fitted parameters of the model of Figure 5a under open-circuit conditions. The geometric capacitance C_g is basically constant, but the other three parameters in the EC show an exponential dependence with the voltage,^{83,89} and they may be expressed as

$$R_1(V) = R_{10} e^{-qV/m_1 k_B T} \quad (12)$$

$$R_3(V) = R_{30} e^{-qV/m_3 k_B T} \quad (13)$$

$$C_1(V) = C_{10} e^{qV/m_c k_B T} \quad (14)$$

Here, m_i ($i = 1, 3$) is an ideality factor for each resistance parameter and m_c for the low-frequency capacitance. In the case of band-to-band recombination at high carrier density it is $m_i = 2$ by the participation of both electrons and holes.⁹⁰ In Figure 6, it is obtained $m_i \approx 2$ in all of the cases, indicating a recombination resistance. On the other hand, C_1 cannot be suitably interpreted as a chemical capacitance.⁹¹

A strong correlation occurs in the low-frequency elements, $m_c \approx m_1$, so that the response time for the slow relaxation phenomenon is a constant independent of the voltage^{88,89,92}

$$\tau_1 = R_1 C_1 \quad (15)$$

Equations 12–15 provide a suitable reference for the construction of a more general model later in this work.

2.4. Inductive Hysteresis. Figure 7b shows the typical capacitive current in a dark perovskite diode, already discussed before. A different type of behavior that produces noncapacitive currents, as shown in Figure 7c, was identified by Garcia-

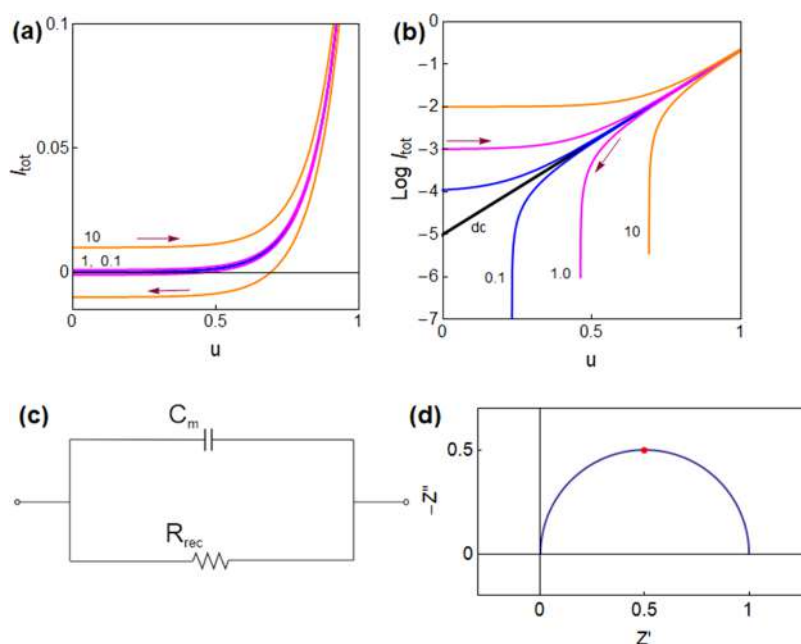


Figure 4. Simulation of hysteresis for a diode characteristic in the dark with a constant capacitor in (a) linear and (b) logarithmic current I_{tot} (in A cm^{-2}) as a function of voltage u (in V). In panel (b), only positive values of current are shown. Parameters $C_m = 0.001 \text{ F cm}^{-2}$, $i_{b0} = 10^{-5} \text{ A cm}^{-2}$, and $V_b = 0.10 \text{ V}$. The scan rate v_i for each curve is indicated in V s^{-1} . The dc line of equilibrium is marked by a black line. (c) Equivalent circuit for small ac impedance. (d) Complex plane impedance spectrum for the parameters $C_m = 0.001 \text{ F cm}^{-2}$ and $R_{\text{rec}} = \Omega \text{ cm}^2$. The red point is at the characteristic frequency $\omega_m = 1/\tau_m = 1/R_{\text{rec}} C_m$.

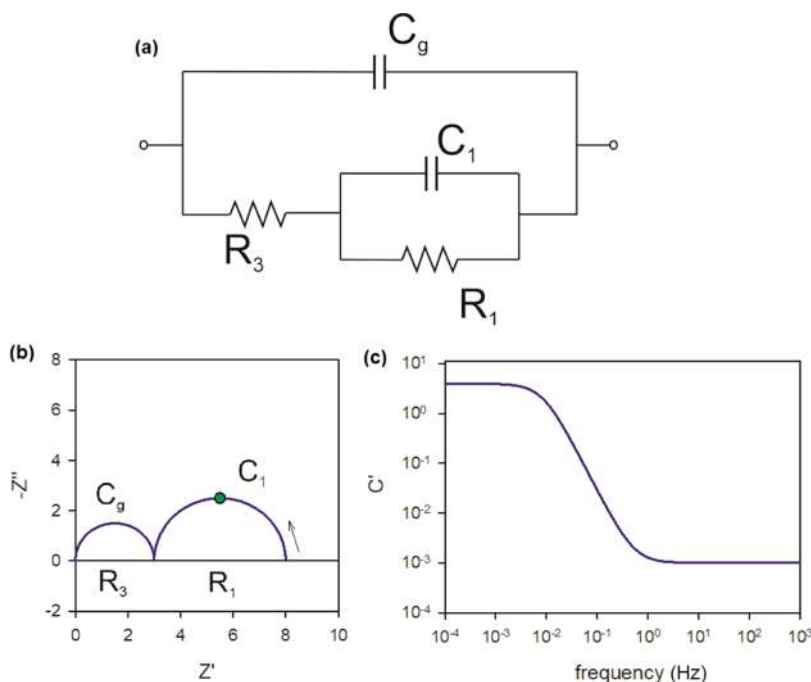


Figure 5. (a) Equivalent circuit and (b) complex plane impedance spectrum (impedances in Ω). The arrow indicates the direction of increasing frequency. The point indicates the angular frequency $1/\tau_1 = 1/R_1 C_1$. (c) Real part of the capacitance vs frequency. Parameters $R_1 = 5 \Omega$, $R_3 = 3 \Omega$, $C_1 = 10 \text{ F}$, and $C_g = 10^{-3} \text{ F}$.

Belmonte and co-workers.²² In the region of separation of the current–voltage curves, the forward current is smaller than the reverse current. In consequence, the current in a voltage sweep changes in the opposite way to the capacitive variation. Figure 7a provides a summary of the different types of currents.⁹³ This behavior was observed in illuminated solar cells,²⁶ as shown in Figure 8, and termed inverted hysteresis.^{24,26,54,55} This feature is

found in many perovskite devices, including solar cells and memristors.³⁶

For the description of inverted hysteresis, we formulate a model that has been denoted a “chemical inductor”.⁹⁴ Chemical inductor is a general denomination for a class of dynamical models that occur in different types of systems (corrosion, batteries, neurons, electrocatalysis, memristors). These dynam-

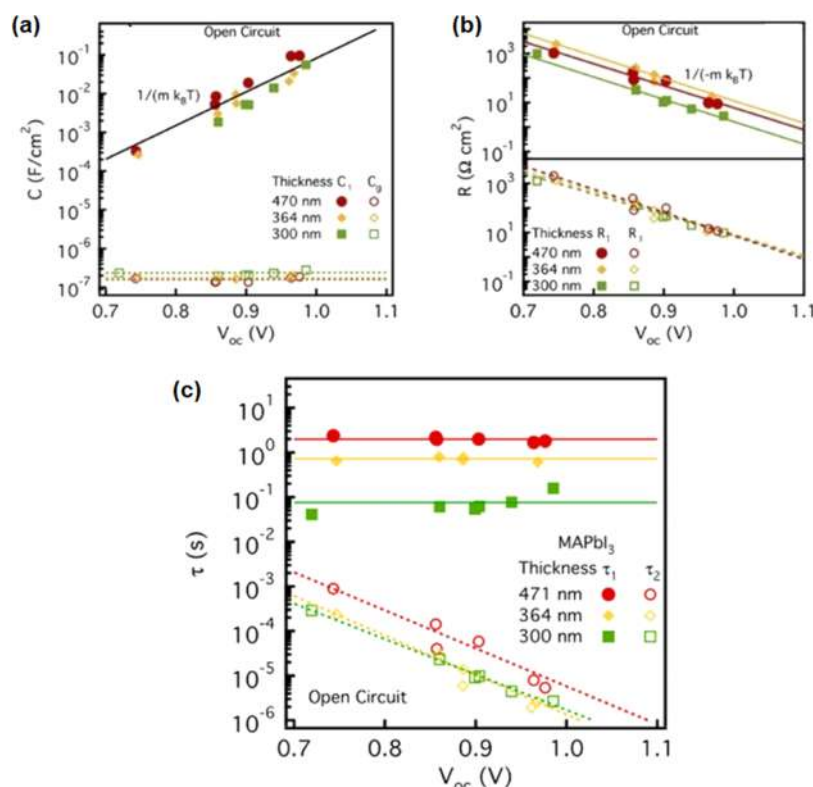


Figure 6. Impedance spectroscopy results of a planar structure FTO/TiO₂/MAPbI₃/Spiro-OMeTAD/Au solar cell under open-circuit conditions. Solid lines correspond to fits using the simplified EC of Figure 5a. (a) Capacitances C₁ (solid circles) and C_g (empty circles), and (b) resistances R₁ (solid circles) and R₃ (empty circles). Solid lines (low-frequency arc) and dashed lines (high-frequency arc) correspond to linear fits. In panel (a), $m = 1.90 \pm 0.17$, and in panel (b), $m = 1.94 \pm 0.08$. (c) Characteristic response time calculated from the RC product for different cell thicknesses. Solid circles, R₁ C₁; empty circles, R₃ C_g. Reproduced from ref 89. Copyright 2016 American Chemical Society.

ical models produce a formal inductive response in impedance and transients *without* the occurrence of an electromagnetic (induction) effect. The chemical inductor is not related to the previously mentioned chemical capacitance, which describes a charge accumulation by the increase of the chemical potential.¹⁴

Here, we apply the chemical inductor to the solar cell.⁹⁴ We modify eq 1 as follows

$$I_{\text{tot}} = C_m \frac{dV}{dt} + i_d \quad (16)$$

Here, i_d is a new variable, a current across the solar cell device that does not respond instantaneously to the applied voltage V . It is regulated by the equation

$$\tau_d \frac{di_d}{dt} = I_a(V) - i_d \quad (17)$$

τ_d is a time constant parameter for the delay of the current. $I_a(V)$ in eq 17 is the dc current that gives the steady-state dependence. Indeed, in equilibrium condition, we have from eqs 16 and 17

$$I_{\text{tot}}(V) = i_d = I_a(V) \quad (18)$$

Throughout this paper, the uppercase currents as $I_a(V)$ are closed expressions of current–voltage, while the lowercase i_d is a variable current determined by the set of differential equations.

To complete the solar cell model, we use for $I_a(V)$ the diode recombination current of eq 5. The current for a constant sweep rate is given by the equations

$$I_{\text{tot}} = C_m v_r + i_d \quad (19)$$

$$V_R \frac{di_d}{dV} + i_d - I_{b0} e^{V/V_b} = 0 \quad (20)$$

where we have defined the sweep velocity parameter as

$$V_R = \tau_d v_r \quad (21)$$

The differential equation, eq 20, is expressed as a function of voltage and can be integrated. For the initial condition $i_d(V = V_0) = i_{d0}$, we obtain

$$i_d(V) = \frac{V_b}{V_b + V_R} I_{b0} e^{V/V_b} + \left(i_{d0} - \frac{V_b}{V_b + V_R} I_{b0} e^{V_0/V_b} \right) e^{(V_0 - V)/V_R} \quad (22)$$

Consider the evolution of the first term on the right side (the second term is a transient related to the initial conditions). If the scan rate is slow $V_R < V_b$, the equilibrium curve is not affected and there is no hysteresis. If the scan rate is fast $V_R > V_b$, we obtain

$$i_d(V) = \frac{V_b}{V_R} I_{b0} e^{V/V_b} \quad (23)$$

We conclude that the current in inductive hysteresis is inversely proportional to the scan rate.

The total current due to the model of eqs 16 and 17 is obtained by inserting eq 22 into eq 19. We observe in eq 23 that the transient inductive current is smaller than the equilibrium current on the forward scan, as shown in Figure 9a,b. We conclude that the eqs 16 and 17 for the chemical inductor

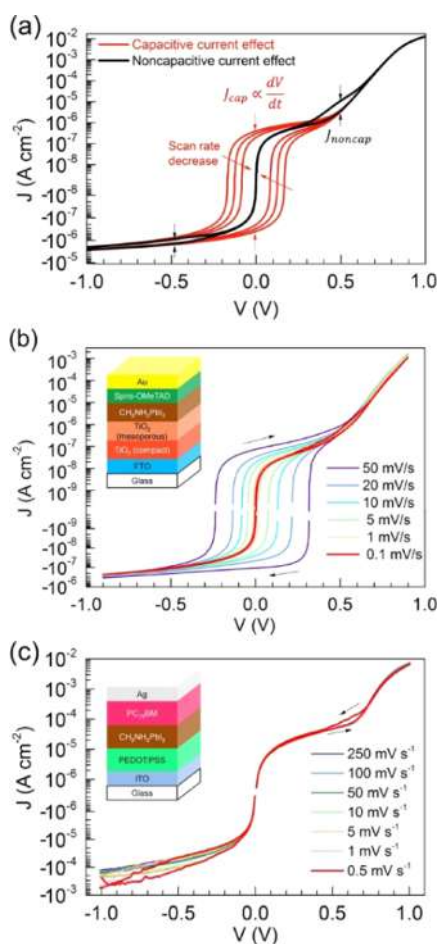


Figure 7. Dark J - V curves at room temperature in logarithm scaled current representation: (a) simulation illustrating different hysteretic effects as a function of the scan rate during the bias sweep in both senses; experimental data from (b) Regular meso (FTO/ c TiO₂/ m TiO₂/MAPbI₃/spiro-OMeTAD/Au) and (c) inverted (ITO/PE-DOT:PSS/MAPbI₃/PC₇₀BM/Ag) perovskite solar cells at different scan rates with corresponding structures sketched in the insets. Reproduced from ref 22. Copyright 2016 American Chemical Society.

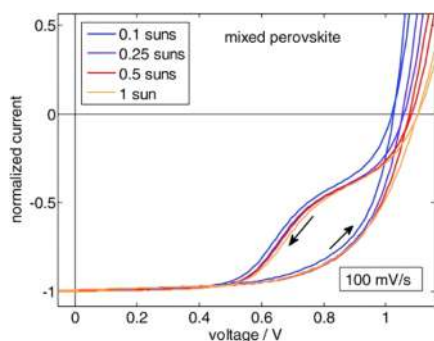


Figure 8. Normalized (at -0.2 V) current-voltage curves of a mixed perovskite device measured at different illumination intensities indicating that the S-shape hysteresis is independent of photogenerated charges. Reproduced by permission from ref 26. Copyright 2016 Wiley.

applied to the solar cell describe well the inverted hysteresis features.

In Figure 9b, we observe that the capacitive current of eq 19 dominates at low voltage. There is a crossing from capacitive to

inductive current. We will describe this phenomenon more completely later based on the experimental results.

2.5. Impedance Properties and Inductive Hysteresis. We analyze the small ac impedance of the chemical inductor model of eqs 16 and 17. We obtain the equations

$$\hat{I}_{\text{tot}} = C_m i \omega \hat{V} + \hat{i}_d \quad (24)$$

$$\tau_d i \omega \hat{i}_d = \frac{1}{R_a} \hat{V} - \hat{i}_d \quad (25)$$

where the resistance is

$$R_a = \left(\frac{\partial I_a}{\partial V} \right)^{-1} \quad (26)$$

We also introduce the chemical inductance

$$L_a = R_a \tau_d \quad (27)$$

and we obtain the impedance function

$$Z = \left(C_m i \omega + \frac{1}{R_a + L_a i \omega} \right)^{-1} \quad (28)$$

This analysis shows that the introduction of the delayed current i_d in eq 17 generates an inductor in series with the resistance in eq 28, cf. eq 11, so that the EC takes the form shown in Figure 9c. The impedance of the inductor element is $Z(\omega) = L_a i \omega$. If the inductance is small, it corresponds to a short circuit and barely changes the RC arc, as shown in the blue spectrum in Figure 9d. But when the inductor is large, it creates a big negative loop passing through the fourth quadrant, in the orange line of Figure 9d, until it closes at the real axis of the complex impedance plane to the value of the dc resistance.

Based on the previous results, we can establish a direct connection between the existence of an inductive branch in the EC of the impedance results and the presence of inverted hysteresis in I - V curves. This has been exposed by Fabregat-Santiago and co-workers,⁹⁵ and it has been explained in general terms by the chemical inductor model.^{25,94} The inductor branch in the EC has a large impact on the solar cell performance as it reduces the recombination resistance and diminishes the power conversion efficiency.^{95,96}

By the relation that we have established of noncapacitive currents (Figures 7–9) with the inductor element, we may classify hysteresis into two distinct types: capacitive hysteresis (regular) and inductive hysteresis (inverted).

2.6. Interpretation of Inductive Current and the Negative Capacitance. The chemical inductor is normally found in conjunction with additional conduction pathways, leading to an extended model. If the ohmic conduction eq 2 is included in the model of eqs 16 and 17, then eq 24 will take the form

$$\hat{I}_{\text{tot}} = C_m i \omega \hat{V} + \frac{\hat{V}}{R_b} + \hat{i}_d \quad (29)$$

When combined with eq 17, this more general model leads to the EC of Figure 10a, which displays a variety of spectra shown in Figure 10b. Again, the negative loop is observed for the larger values of the inductor parameter. Figure 10c indicates that the crossing to the fourth quadrant occurs when the condition

$$\tau_d = \frac{L_a}{R_a} > \tau_a = R_a C_a \quad (30)$$

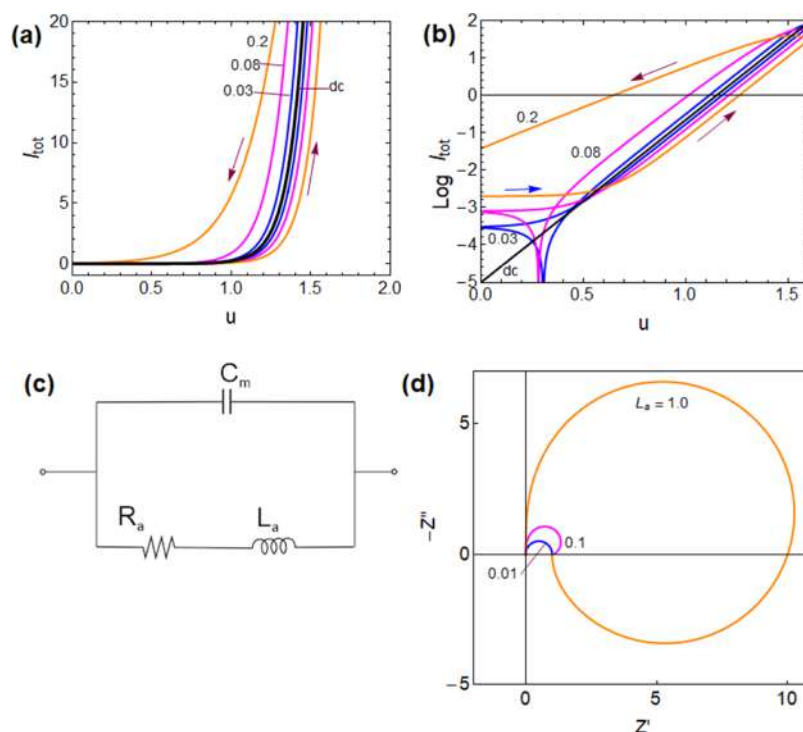


Figure 9. Simulation of hysteresis for a diode characteristic in the dark with a constant capacitor and a chemical inductor in (a) linear and (b) logarithmic current I_{tot} (in A cm^{-2}) as a function of voltage u (in V). In panel (b), the absolute values of current are shown. Parameters $C_m = 0.01 \text{ F cm}^{-2}$, $i_{b0} = 10^{-5} \text{ A cm}^{-2}$, $V_b = 0.10 \text{ V}$, and $\tau_d = 1 \text{ s}$. The scan rate v_r is indicated in V s^{-1} . The dc line of equilibrium is indicated by a black line. The blue arrow in panel (b) indicates a capacitive hysteresis region. (c) Equivalent circuit and (d) impedance spectra for $C_m = 0.1 \text{ F cm}^{-2}$, $R_a = 1 \text{ } \Omega$, and L_a as indicated (H).

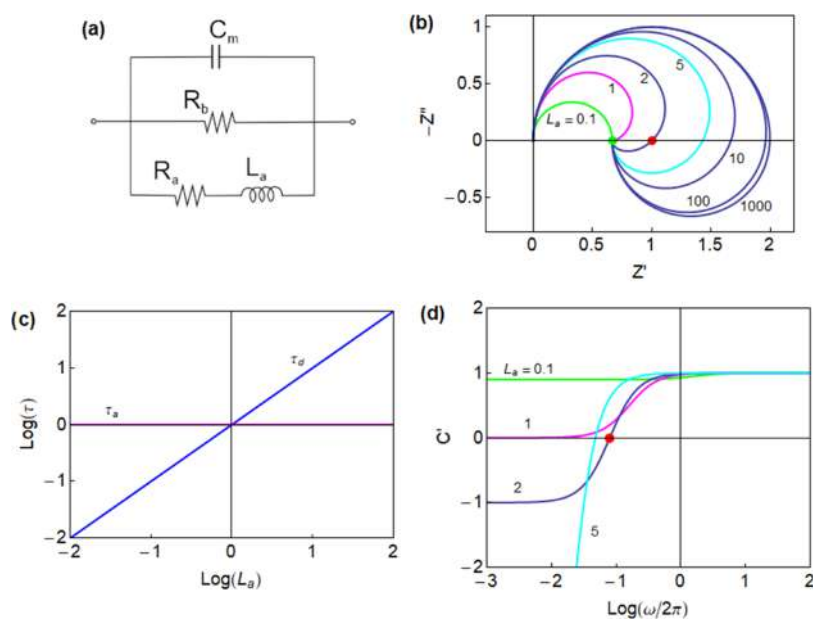


Figure 10. (a) Equivalent circuit of the chemical inductor with capacitance and additional conductance. (b) Impedance spectra generated for $C_m = 1 \text{ F}$, $R_a = 1 \text{ } \Omega$, $R_b = 2 \text{ } \Omega$, and L_a as indicated (H). The green dot is the dc resistance at $\omega = 0$, and the red dot is the resistance at the intercept when the spectrum crosses the real axis Z' . (c) Time constants $\tau_a = R_a C_m$ and $\tau_d = L_a/R_a$ for a varying inductance. The negative loop in the complex plane occurs when $\tau_d > \tau_a$ is satisfied. (d) Representation of the real part of the capacitance as a function of frequency. The red point indicates the crossing of the horizontal axis.

is satisfied.⁹⁴ In eq 29, the decrease of the current of the chemical inductor at increasing scan rate is limited by the parallel branch R_b .²⁵

The complex capacitance $C(\omega)$ is defined from the impedance as

$$C(\omega) = \frac{1}{i\omega Z(\omega)} \quad (31)$$

The real part of the capacitance is denoted $C'(\omega) = \text{Re}[C(\omega)]$. In the capacitive model of Figure 5, the total

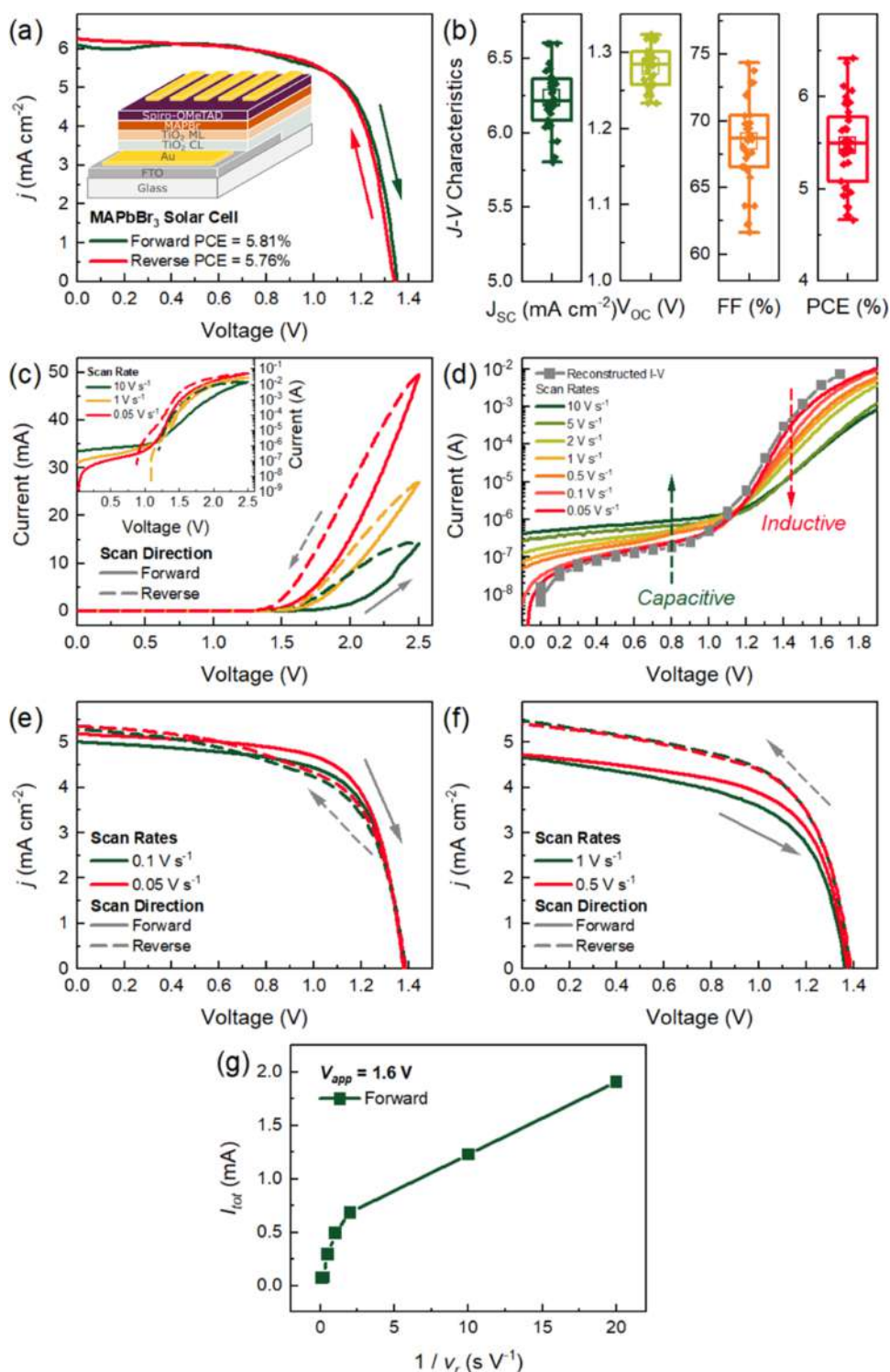


Figure 11. (a) Characteristic I - V curve of the MAPbBr₃ solar cell under 1 sun illumination exhibiting inverted hysteresis with the inset showing the schematic diagram of the device configuration. (b) I - V characteristic parameter statistics of 34 devices measured in the reverse scan direction. (c) Forward and reverse I - V scans with varying scan rates exhibiting inverted hysteresis measured inside a nitrogen-controlled glovebox under dark conditions. (d) Evolution of hysteresis in the forward direction in log vertical scale in dark. (e-f) Hysteresis under illumination conditions. (g) Current in forward for inverted hysteresis in the dark at 1.6 V vs reciprocal scan rate.

capacitance is strictly positive, Figure 5c. Figure 10d shows an interesting phenomenon. When the loop in the fourth quadrant occurs in the complex plane impedance spectrum, the complex capacitance becomes negative. We arrive at the conclusion that the chemical inductor generates the feature of a negative capacitance at a low frequency that has been extensively

reported in halide perovskite solar cells.^{46,48,85,97-101} The negative capacitance can be described by a positive chemical inductor that arises from the model of eqs 16 and 17. A truly negative capacitance parameter is not necessary.

The chemical inductor is generally obtained from the delay eq 17, as shown above.¹⁰² But what is the interpretation of this

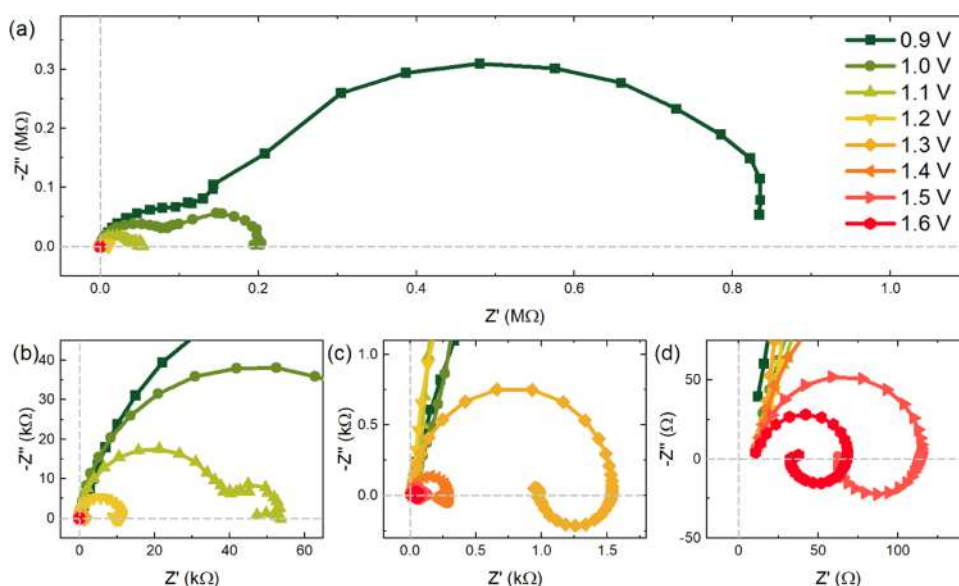


Figure 12. (a) Representative IS spectral evolution of the MAPBr solar cell at $V_{\text{app}} = 0.9\text{--}1.6$ V under dark conditions. Panels (b)–(d) show different magnifications around the origin.

delay effect in halide perovskites? Since the observation of the negative capacitance is widespread, many different explanations are provided. Some examples are the physical surface polarization model,^{77,103} the changing environment of ions when their occupation at the double layer is modified by the photovoltage or polarization,^{92,104,105} and the modulation of electronic conduction or recombination currents.^{53,97,99,100,106–111} Most of these models have in common that a slow step of ionic displacement determines a faster step of electronic current recombination or transfer at the contact. These different models presented for negative capacitances and inductive hysteresis are compatible with the general operation principle of the chemical inductor. In fact, the model of a chemical inductor originates from a voltage-gated ion channel in the neuron membrane originally described by Hodgkin and Huxley.^{63,64} It describes well a voltage-gated electronic current at the bulk of the surface of the solar cell.^{53,98,108,109} However, the molecular mechanism of this behavior has not been determined yet in perovskite solar cells.

3. METHODS

3.1. MAPBr Solar Cell Fabrication. The fluorine-doped tin oxide (FTO) substrates were partially etched with zinc powder and 2 M HCl solution. The etched samples were brushed to mechanically remove the remaining residues of the etching procedure, then were sonicated for 15 min each in deionized water with Hellmanex detergent solution, acetone, and isopropyl alcohol, respectively. The cleaned substrates are then dried using a nitrogen gun.

In preparation for the electron selective titanium dioxide (TiO_2) compact layer deposition, the cleaned substrates were subjected to ultraviolet (UV) ozone treatment for 15 min to further remove organic contaminants on the substrate surface. The TiO_2 compact layer was then deposited via spray pyrolysis of 1:9 titanium(IV) diisopropoxide bis(acetylacetonate) (75% solution in 2-propanol, Sigma-Aldrich) (60% in acetylacetonate)/ultrapure ethanol at 450 °C with oxygen as carrier gas. The TiO_2 compact layer is then kept at 450 °C for 35 min before letting the samples cool down to room temperature. Another UV ozone

treatment for 15 min was conducted on samples with the TiO_2 compact layer to ensure ultraclean surface prior to the deposition of the TiO_2 mesoporous layer. A 100 μL diluted TiO_2 paste (Dyesol) (150 mg/1 mL ultrapure ethanol) was then spin-coated onto the TiO_2 compact layer at a speed of 2000 RPM, acceleration of 2000 RPM/s with a duration of 10 s. The deposited TiO_2 mesoporous layer was annealed under ambient conditions at the following temperature, ramp time, and dwell time: 370 °C with 40 min ramp for 20 min, 470 °C with 25 min ramp for 10 min, and 500 °C with 10 min ramp for 30 min.

Once the annealing treatment of the TiO_2 mesoporous layer was completed, the samples were cooled down to 150 °C and were immediately transferred inside a glovebox in preparation for the MAPBr deposition. A 1.4 M MAPBr precursor solution is prepared using PbBr_2 (>98%, TCI) and MABr (>99.99%, Greatcell Solar) in 1:4 dimethylsulfoxide (DMSO) ($\geq 99.9\%$, Sigma-Aldrich)/*N,N*-dimethylformamide (DMF) (99.8%, Sigma-Aldrich) solution. A 50 μL MAPBr perovskite solution was statically spin-coated onto the TiO_2 mesoporous layer via a two-step antisolvent method: 1000 RPM for 10 s, then 4000 RPM for 40 s. A 100 μL toluene (99.8%, Sigma-Aldrich) antisolvent was injected 22 s before spin coating ended. The samples were then annealed at 100 °C for 30 min.

The hole selective lithium-doped 2,2',7,7'-tetrakis[*N,N*-di(4-methoxyphenyl)amino]-9,9'-spirobifluorene (Spiro-OMeTAD) was deposited on top of the annealed perovskite layer. A 72.3 mg Spiro-OMeTAD in 1 mL chlorobenzene (99.8%, Sigma-Aldrich), 28.8 μL 4-*tert*-butylpyridine (98%, Sigma-Aldrich), and 17.5 μL of a stock solution of 520 mg lithium bis-(trifluoromethyl sulfonyl) imide (99.95%, Sigma-Aldrich) in 1 mL acetonitrile (99.8%, Sigma-Aldrich) was prepared. A 50 μL lithium-doped Spiro-OMeTAD solution was dynamically spin-coated at 4000 RPM, 800 RPM/s for 30 s. Finally, an 85 nm gold contact was thermally evaporated using a commercial Oerlikon Leybold Univex 250.

3.2. MAPBr Solar Cell Characteristic J – V Curves and Statistics. The characteristic J – V curves of the MAPBr solar cells were measured with a mask aperture area of 0.120 cm^2 using a computer-controlled Keithley 2400 under a simulated AM1.5 solar spectrum from an ABET Technologies Sun 2000

solar simulator. The MAPBr solar cells had total active areas of $\sim 0.257 \text{ cm}^2$.

3.3. Impedance Spectroscopy Measurement. All electrical measurements were conducted inside a nitrogen-controlled glovebox under dark conditions using Autolab PGSTAT204. The voltage-dependent IS response was measured via a sequence of chronoamperometry (CA) for 5 s, subsequently followed by IS with a frequency range of 1 MHz to 0.02 Hz and a perturbation amplitude of 0.01 V. The CA–IS sequence was carried out at varying applied voltages (V_{app}) from 0 to 2 V at 0.1 V increments.

4. RESULTS AND DISCUSSION

Figure 11 shows the electrical characterization of the fabricated MAPbBr₃ solar cells. I – V characteristics and device statistics are presented in Figure 11a,b. The power conversion efficiencies approaching 6% in the forward and reverse scan directions are within the normal values reported for this formulation.⁶⁹ Devices with optimized contacts can show still higher efficiency.^{112,113}

The current–voltage curves in the dark at different scan rates in Figure 11c show intense inverted hysteresis and correspondingly exhibit decreasing current levels with increasing scan rates, as indicated in Figure 11d.^{25,53} The log scale representation of Figure 11d reveals a region of capacitive hysteresis at low voltage, as announced in Figure 9 before. A crossing point is observed in which a transition from regular to inverted hysteresis occurs. This transition has been applied recently to explain the negative spikes observed in transient time measurements.¹⁰² Figure 11g shows that the forward current is inversely proportional to the scan rate for the slow voltage sweeps, as predicted in eq 23 for the chemical inductor. For faster scan rates, the current tends to reach a minimum due to parallel pathways, as discussed before in eq 29. A similar behavior is observed in the current–voltage curves under illumination at different scan rates. However, the crossing point under light is not fixed. It shifts from values close to 0 V at low scan rates (Figure 11e) to higher values with an increase in the sweep rate. At fast scan rates (Figure 11f), the crossing point is not observed and the hysteresis is only inductive. Since this additional effect complicates the analysis in the following, only data in the dark will be discussed.

These properties can be put in correspondence with the stabilized impedance spectra shown in Figure 12. The fully capacitive spectra, consisting of several arcs in the low-voltage region (Figure 12a,b), correspond to the regular hysteresis domain. In the high voltage region, a large inductive feature appears (Figure 12c,d) that causes a negative transient current resulting in an inverted hysteresis. These separate features have been explained in Section 2. As described earlier, ionic charges can modulate the carrier extraction rate or recombination current. As the ionic motion is much slower than electronic response, a delay of the electrical current is observed that causes capacitive and inductive components.

4.1. Dynamical Model. We present here an advanced dynamical model that enables us to correlate both the results of impedance and current–voltage curves and obtain a physical interpretation of the evolution of parameters with the voltage. The model is formulated as a set of dynamical equations valid for any type of perturbation. These equations contain the minimal components to describe all of the features shown in Figures 11 and 12, based on the experience in different capacitive and inductive components and series and parallel elements that has

been summarized in Section 2. This model goes further than combining the component parts as it needs to account for the data across the whole voltage range, and especially it must explain the emergence of the inductor and the disappearance of the low-frequency impedance arc in Figure 12. The model is the first of its kind that introduces a voltage divisor to deal with two impedance arcs.⁵¹

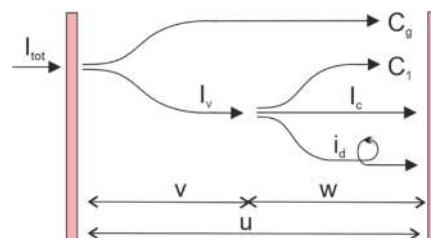


Figure 13. Scheme of the dynamical model showing total current I_{tot} and voltage u , internal voltages $u = v + w$, conduction (I_v , I_c , i_d), and capacitive (C_g , C_1) currents between the current collector plates. The lines arriving at the right contact indicate the dc current.

The physical basis for the model is shown in Figure 13. The total current flowing through the device is divided into the following components:

- (1) A part of I_{tot} is a displacement current that charges the geometrical capacitance of the perovskite material (C_g). The remaining current I_v will be divided into three branches:
- (2) Charging the surface capacitance C_1 .
- (3) Extracting rapid current I_c at the contact.
- (4) Extracting current slowly via an ion-modulated current i_d .

Therefore, the model equations are

$$I_{\text{tot}} = C_g \frac{du}{dt} + I_v(v) \quad (32)$$

$$I_v(v) = \frac{dQ_s(w)}{dt} + I_c(w) + i_d \quad (33)$$

$$\tau_d \frac{di_d}{dt} = I_d(w) - i_d \quad (34)$$

The external variables are the total current I_{tot} and voltage u . The voltage is divided into two internal parts, v and w , that correspond to bulk and surface potential differences, respectively, and satisfy

$$u = v + w \quad (35)$$

The internal currents $I_v(v)$ and $I_c(w)$ are instantaneous functions of the respective voltage, while i_d is a variable current that is delayed by a characteristic time τ_d due to ionic effects, as described in Section 2.4.⁹⁴ Hence eq 34 is the standard form of the chemical inductor introduced in eq 17. The model also includes a surface charge function $Q_s(w)$ and the stationary value of the delayed current $I_d(w)$.⁵¹

We have noted in eqs 12–14 that the resistances and capacitance in perovskite solar cells have exponential dependences on voltage, and some of them are correlated. Based on these observations, we assume the exponential dependence in the currents

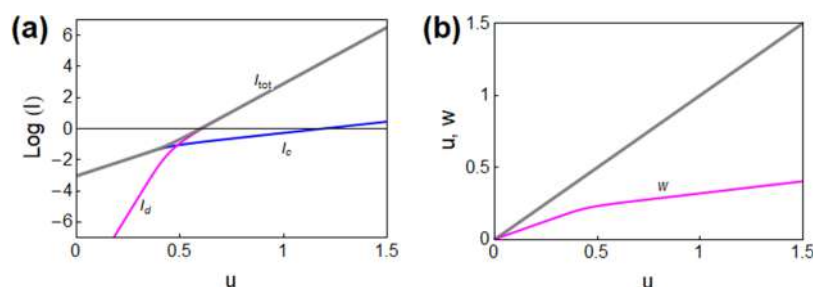


Figure 14. Model simulation. (a) Stationary current–voltage curve and the component currents and (b) distribution of internal voltage. Parameters: $I_{v0} = 10^{-3}$, $I_{c0} = 0.9 \times 10^{-3}$, $I_{d0} = 10^{-11}$, $V_b = 0.05$, and $V_d = 0.01$. Currents in A and voltages in V.

$$I_v(v) = I_{v0}e^{v/V_b} \quad (36)$$

$$I_c(w) = I_{c0}e^{w/V_b} \quad (37)$$

$$I_d(w) = I_{d0}e^{w/V_d} \quad (38)$$

Here I_{v0} , I_{c0} , and I_{d0} are prefactors, and V_b and V_d are ideality factors⁸² with a dimension of voltage.

According to Figure 13 the partial currents satisfy the following equation in dc conditions

$$I_v(u - w) = I_c(w) + I_d(w) \quad (39)$$

By eq 39 the relation of external voltage u to internal potential is

$$u = V_b \ln \left(\frac{I_{c0}}{I_{v0}} e^{2w/V_b} + \frac{I_{d0}}{I_{v0}} e^{w/V_d} \right) \quad (40)$$

where

$$V_c^{-1} = V_d^{-1} + V_b^{-1} \quad (41)$$

The total current is shown in Figure 14a and the distribution of the internal voltages in Figure 14b. Since $V_d < V_c$, the delayed current I_d , which starts at a low value in Figure 14a, overcomes the direct recombination current I_c at the internal voltage value given by the parameter

$$w_T = \left(\frac{1}{V_d} - \frac{1}{V_b} \right)^{-1} \ln \left(\frac{I_{c0}}{I_{d0}} \right) \quad (42)$$

4.2. AC Impedance Model. For the interpretation of impedance spectroscopy of our experimental results, we develop eqs 32–34 into the small perturbation equations that become

$$\hat{I}_{\text{tot}} = C_g \frac{d\hat{u}}{dt} + \frac{1}{R_3} \hat{v} \quad (43)$$

$$\frac{1}{R_3} \hat{v} = C_1 \frac{d\hat{w}}{dt} + \frac{1}{R_1} \hat{w} + \hat{i}_d \quad (44)$$

$$L_a \frac{d\hat{i}_d}{dt} = \hat{w} - R_a \hat{i}_d \quad (45)$$

Here, the new circuit elements have the form

$$C_1 = \frac{dQ_s}{dw} \quad (46)$$

$$R_1 = \left(\frac{dI_c}{dw} \right)^{-1} \quad (47)$$

$$R_3 = \left(\frac{dI_v}{dv} \right)^{-1} \quad (48)$$

$$R_a = \left(\frac{dI_d}{dw} \right)^{-1} \quad (49)$$

$$L_a = \tau_d \left(\frac{dI_d}{dw} \right)^{-1} \quad (50)$$

C_1 is a capacitance related to the surface charging,^{86,114} R_1 , R_3 , and R_a are variable resistances connected to the currents of eqs 36–38, and L_a is an inductor associated with the delayed current of eq 34. Now the different resistances can be calculated as a function of voltage.

$$R_1 = \frac{V_b}{I_{c0}} e^{-w/V_b} \quad (51)$$

$$R_a = \frac{V_d}{I_{d0}} e^{-w/V_d} \quad (52)$$

$$R_3 = \frac{V_b}{I_{v0}} e^{-v/V_b} \quad (53)$$

Noting the correlations of C_1 and R_1 commented in Figure 6, we write

$$C_1 = C_{10} e^{w/V_b} \quad (54)$$

We have the characteristic times

$$\tau_1 = R_1 C_1 \quad (55)$$

$$\tau_a = R_a C_1 \quad (56)$$

$$\tau_d = \frac{L_a}{R_a} \quad (57)$$

By taking the Laplace transform of eqs 43–45 in terms of the variable $s = i\omega$, the calculation of the impedance $Z = \hat{u}/\hat{I}_{\text{tot}}$ gives the result

$$Z(s) = \left[C_g s + \frac{1}{R_3 + \frac{1}{C_1 s + \frac{1}{R_1 + \frac{1}{R_a + L_a s}}}} \right]^{-1} \quad (58)$$

The impedance in eq 58 becomes that of the EC of Figure 15, with the addition of a constant series resistance R_s . The branch formed by R_a and L_a is the arrangement of the chemical inductor that describes delayed surface-controlled recombination as in Section 2.5.

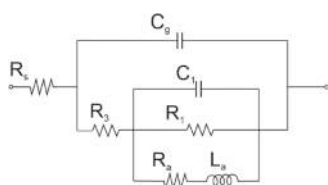


Figure 15. Schematic diagram of the general equivalent circuit model.

4.3. Obtaining the Impedance Parameters. The analysis of the spectra of Figure 12 cannot be done by the direct fitting of the full equivalent circuit of Figure 15 since the elements of the circuit are not present in the entire voltage range. Different simplifications of Figure 15 are used as separate voltage ranges as shown in Figure 16, which displays the EC adopted in the various domains for the spectral analysis of IS data in Figure 12.

At low voltages in Figure 16a, the inductor impedance is large, and we obtain the double RC feature of Figure 16a that was shown previously in Figure 5, see the spectra Figure 16b,c. The intermediate region of voltages in Figure 16d is a transition region where all of the elements in the EC are present. The spectra in Figure 16e,f show the replacement of the low-frequency arc by an incipient inductive feature. At high voltages in Figure 16g, the capacitive arc associated with C_1 is not observed, and it is replaced by the chemical inductor feature of Figure 10. Now the inductive arc is well developed in the experimental spectra in Figure 16h,i. An additional parallel shunt resistance of constant value R_{sh} is used in the fitting as described in the Supporting Information. The fits capture well the features of the impedance spectra as shown in Figure 16 with the resulting EC parameters summarized in Figure 17: resistances

(Figure 17a), effective capacitances (Figure 17b), effective inductance (Figure 17c), and the corresponding time constants (Figure 17d).

In Figure 17, we find well-established features of the impedance parameters of the low-voltage region by comparison to Figure 6. The R_1 and R_3 decrease exponentially with voltage, with similar slopes, as in Figure 6b. The R_a also decreases with voltage but with a different slope, and it is correlated to L_a , which makes τ_d a constant as assumed in the model. The C_1 increases exponentially, as in Figure 6a, inversely correlated to R_1 , hence the characteristic time τ_1 in Figure 17d is a constant as in Figure 6c.

4.4. Transition from Capacitor to Inductor. We now discuss the properties of the chemical inductor observed in Figure 17. The change from the capacitor to the inductor is controlled by the relation of the time constants, as explained in Figure 10. When $\tau_d > \tau_a$, there is a transition of the spectra in the low-frequency range, with the appearance of the inductor in the fourth quadrant (producing a negative capacitance feature).

Let us write the time constant τ_1 using eqs 46, 47, and 55

$$\tau_1 = \frac{dQ_s}{dw} \frac{1}{\frac{dI_c}{dw}} = \frac{dQ_s}{dI_c} \quad (59)$$

We obtain that the ionic charging of the interface occurs with the time constant τ_1 as follows

$$Q_s \approx \tau_1 I_c \quad (60)$$

We note the property of nearly continuity of characteristic times obtained in Figure 17d

$$\tau_1 \approx \tau_d \quad (61)$$

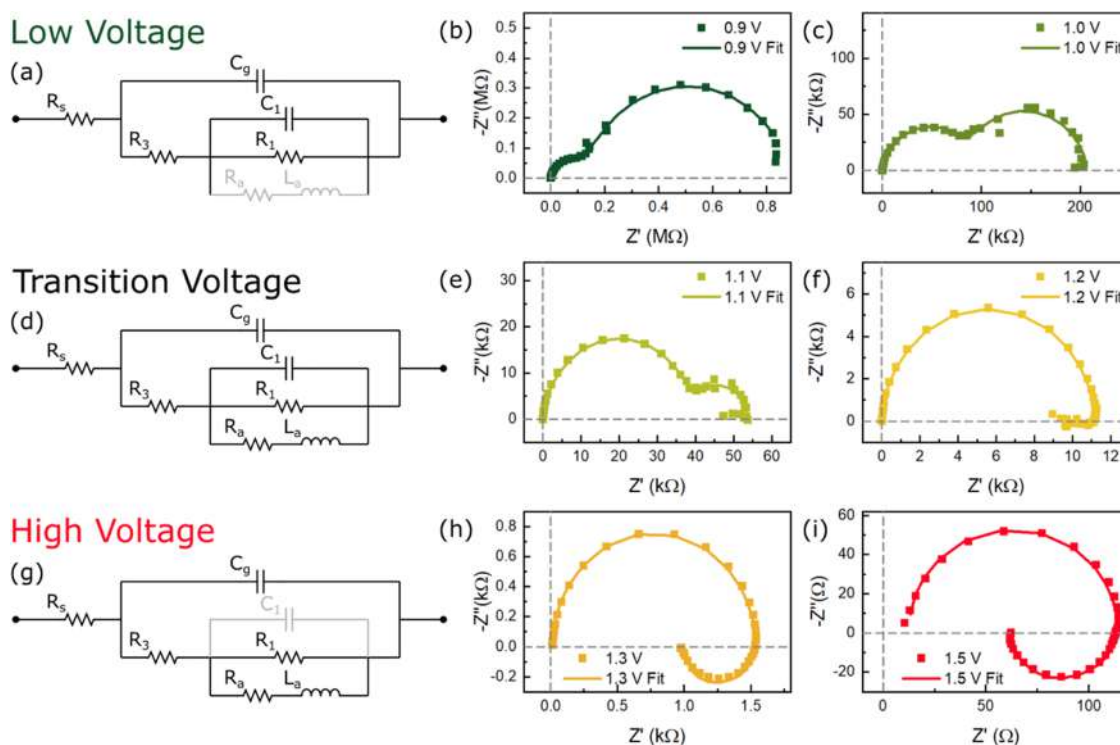


Figure 16. Individual representative IS spectral evolution of the MAPBr solar cell at varying applied voltages (V_{app}) under dark conditions exhibiting (b, c) the fully capacitive regime at low voltages ($V_{app} < 1.1$ V), (e, f) the region of transformation (1.1 V $\leq V_{app} \leq 1.2$ V), and (h, i) the inductive regime at high voltages ($V_{app} > 1.2$ V) with the corresponding equivalent circuits (a, d, g), respectively.

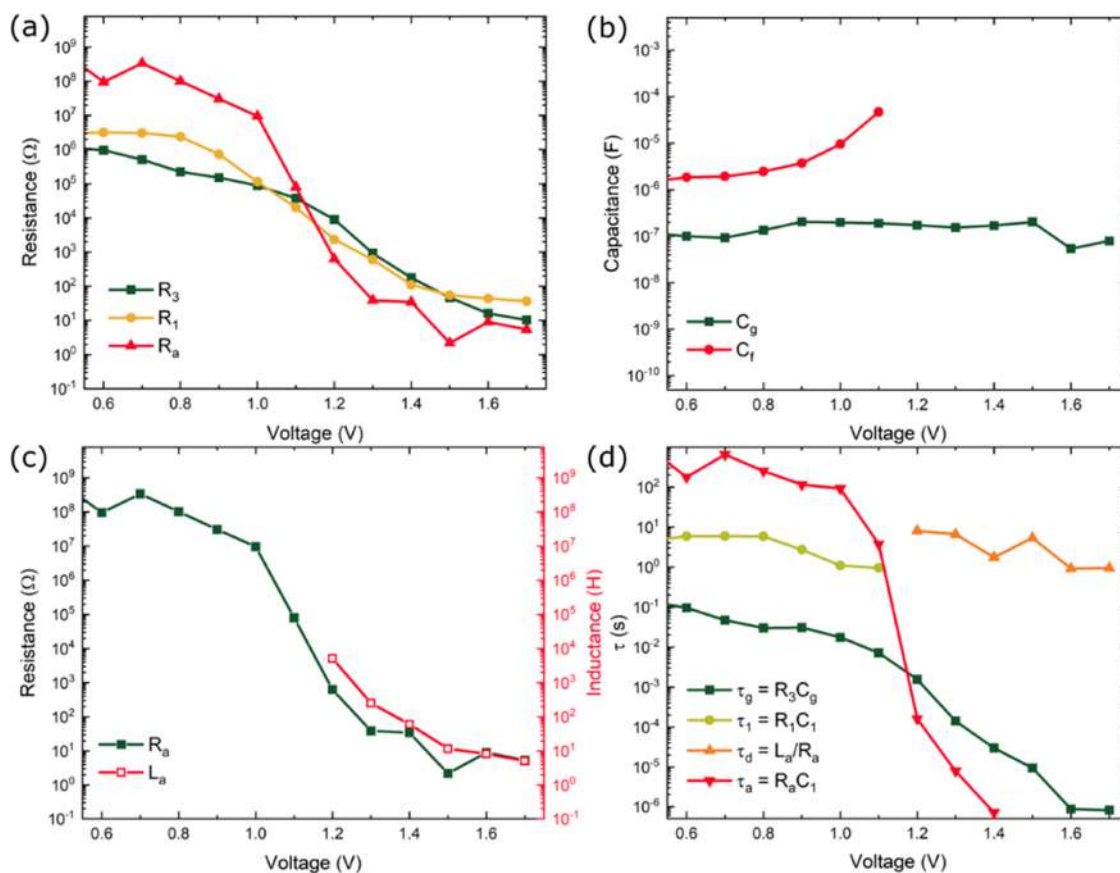


Figure 17. Voltage-dependent evolution of the (a) resistances, (b) capacitances, (c) inductance at high voltage, and (d) the corresponding time constants resulting from the fitting using eq 12 with a consistent shunt resistance of $\sim 1.24 \times 10^9 \Omega$ throughout the voltage range.

We have remarked before that the capacitor C_1 vanishes when the inductive process appears. The match of time constants in eq 61 explains the relation between them. According to the proposed interpretations,^{53,59,88,89} the current I_c in Figure 13 is a surface recombination process observed at low voltages, influenced by ionic changing from the bulk via the ionic-electronic capacitance C_1 . The delayed current i_d in Figure 13 dominant at high voltage is a recombination current influenced by ionic transport to the interface. Hence L_a and C_1 are not completely independent processes: they both relate to the ionic influence on recombination. Both correspond to a similar ionic-controlled recombination, one is capacitive and the other inductive. Therefore, they are represented by different branches in Figures 13 and 15. The connection between capacitive and inductive time constants is also found in a surface polarization model in which the slow variable that produces the chemical inductor is a surface voltage.¹⁰³

By the eqs 60 and 61, we write the prefactor of the capacitor in eq 54 as

$$C_{10} = \frac{I_{c0}\tau_d}{V_b} \quad (62)$$

and we get the charging function as

$$Q_s = I_{c0}\tau_d e^{w/V_b} \quad (63)$$

The EC elements are then plotted in Figure 18a and reproduce the tendencies of the experimental features observed in Figure 17. The model accounts successfully for the voltage variation of the impedance parameters.

In addition, the model shows that the correlation^{83,89,92} often observed on R_1 and R_3 is based on eq 39 and occurs when there are no alternative pathways to the current, e.g., while $I_d(w)$ is small and the shunt resistance is large.

The characteristic times are shown in Figure 18b. As already discussed, there is a continuity of $\tau_1 = \tau_d$ in the transition from capacitive to inductive impedance spectra. It can be stated that

$$\tau_a = R_a C_1 = \tau_d \frac{I_{c0} V_d}{I_{d0} V_b} e^{(\frac{1}{V_b} - \frac{1}{V_d})w} \quad (64)$$

As already mentioned, the transition where the impedance enters the fourth quadrant occurs when the time $\tau_a < \tau_d$.⁶⁷ However, if $\tau_a > \tau_d$ at all voltages, there will not be a domain of negative capacitance effect. The condition (eq 64) therefore explains in which cases there will be an observation of inductive or negative capacitance features.

4.5. Change of Type of Hysteresis. Finally, we aim to explain the transition from regular to inverted hysteresis observed in the current–voltage curves of Figure 11d, corresponding to the change of the impedance from capacitive to inductive response. We formulate the dynamical equations for the stimulus of a voltage sweep as in eq 6

$$u = v_t t \quad (65)$$

Hence, we obtain

$$I_{\text{tot}} = C_g v_t + C_1(w) v_t \frac{dw}{du} + I_c(w) + I_v(v) \quad (66)$$

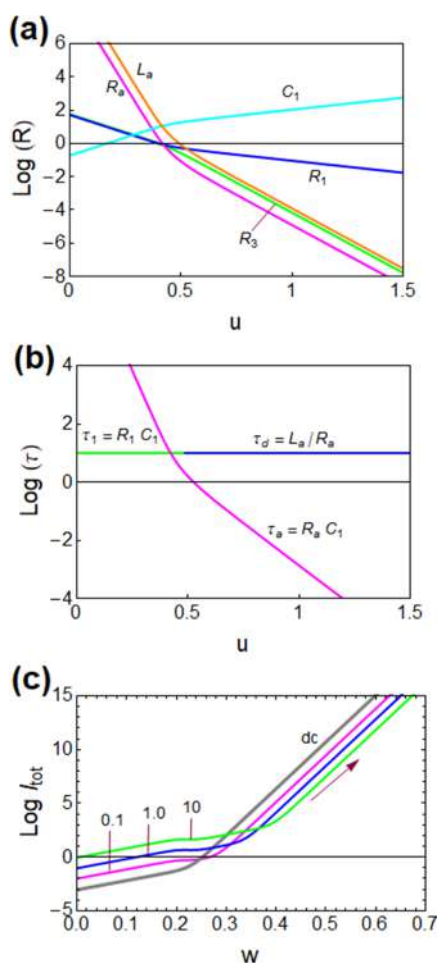


Figure 18. Simulation of the model. (a) Impedance parameters, C in F, R in Ω , L in H, current in A, and voltages in V. (b) Characteristic times (s), and (c) current–voltage curves at different scan rates $\nu_r = 0.1, 1.0$, and 10 (V s^{-1}) as indicated. The gray line is the dc stationary current. Parameters: $I_0 = 10^{-3}$, $I_a = 0.9 \times 10^{-3}$, $I_{a0} = 10^{-11}$, $V_b = 0.05$, $V_d = 0.01$, and $\tau_d = 10$ s. Currents in A and voltages in V.

$$\tau_d \nu_r \frac{dw}{du} \frac{dI_d}{dw} = I_d(w) - I_d \quad (67)$$

where

$$\frac{dw}{du} = \frac{I_{c0} e^{2w/V_b} + I_{d0} e^{w/V_c}}{2I_{c0} e^{2w/V_b} + \frac{V_b}{V_c} I_{d0} e^{w/V_c}} \quad (68)$$

The differential equation (eq 67) can be solved for the given ν_r and inserted into eq 66 to provide the total current. The resulting current–voltage curves at forward scan are shown in Figure 18c and reproduce the crossing due to the change of hysteresis type observed in Figure 11d.

5. CONCLUSIONS

We formulated a dynamical model for the external current, the voltage, and a few internal variables of a solar cell, to describe impedance spectroscopy and hysteresis in current–voltage curves of halide perovskite solar cells that show a transition from a capacitive domain at low voltage to an inductive domain at high applied voltage. The model reproduces the main experimental characteristics of impedance, steady-state current–voltage, and the curves under different sweep rates.

It is well known that the capacitive excess current is proportional to the scan rate; we showed that the inductive current is inversely proportional to the scan rate.

The application of the model provides a great degree of control over the kinetic properties of halide perovskite solar cells, including the amount and type of hysteresis that may be expected from the measurement of impedance spectroscopy at different voltages. By determining a few parameters in an impedance spectroscopy measurement, it is now possible to predict the amount and type of hysteresis that the perovskite solar cell device will have. Furthermore, one can correlate the hysteresis response with the device materials properties via the impedance parameters that are obtained in the equivalent circuit.

The general model can track a transformation of the low-frequency capacitor into a chemical inductor, both related to the ionic-controlled surface recombination process. The different kinetic properties are regulated by the variation of certain time constants that determine the dominant impedance response. This explains why the inductive feature may not produce a negative capacitance, so that hysteresis will remain regular in the whole voltage range.

ASSOCIATED CONTENT

Supporting Information

The Supporting Information is available free of charge at <https://pubs.acs.org/doi/10.1021/acs.jpcc.2c02729>.

Mathematica program for calculations and data fitting program (PDF)

AUTHOR INFORMATION

Corresponding Authors

Antonio Guerrero – Institute of Advanced Materials (INAM), Universitat Jaume I, 12006 Castelló, Spain; orcid.org/0000-0001-8602-1248; Email: aguerrer@uji.es

Juan Bisquert – Institute of Advanced Materials (INAM), Universitat Jaume I, 12006 Castelló, Spain; orcid.org/0000-0003-4987-4887; Email: bisquert@uji.es

Author

Cedric Gonzales – Institute of Advanced Materials (INAM), Universitat Jaume I, 12006 Castelló, Spain; orcid.org/0000-0002-6550-2007

Complete contact information is available at: <https://pubs.acs.org/doi/10.1021/acs.jpcc.2c02729>

Notes

The authors declare no competing financial interest.

ACKNOWLEDGMENTS

The authors thank the financial support by the Ministerio de Ciencia e Innovación of Spain (MICINN) project PID2019-107348GB-I00.

REFERENCES

- (1) Kojima, A.; Teshima, K.; Shirai, Y.; Miyasaka, T. Organometal halide perovskites as visible-light sensitizers for photovoltaic cells. *J. Am. Chem. Soc.* **2009**, *131*, 6050–6051.
- (2) *Organic–Inorganic Halide Perovskite Photovoltaics: From Fundamentals to Device Architectures*, Park, N.-G.; Grätzel, M.; Miyasaka, T., Eds.; Springer, 2016.

- (3) Nayak, P. K.; Mahesh, S.; Snaith, H. J.; Cahen, D. Photovoltaic solar cell technologies: analysing the state of the art. *Nat. Rev. Mater.* **2019**, *4*, 269–285.
- (4) Kim, J. Y.; Lee, J.-W.; Jung, H. S.; Shin, H.; Park, N.-G. High-Efficiency Perovskite Solar Cells. *Chem. Rev.* **2020**, *120*, 7867–7918.
- (5) Saliba, M.; Matsui, T.; Domanski, K.; Seo, J.-Y.; Ummadisingu, A.; Zakeeruddin, S. M.; Correa-Baena, J.-P.; Tress, W. R.; Abate, A.; Hagfeldt, A.; Grätzel, M. Incorporation of rubidium cations into perovskite solar cells improves photovoltaic performance. *Science* **2016**, *354*, 206–209.
- (6) Saliba, M.; Matsui, T.; Seo, J.-Y.; Domanski, K.; Correa-Baena, J.-P.; Nazeeruddin, M. K.; Zakeeruddin, S. M.; Tress, W.; Abate, A.; Hagfeldt, A.; Grätzel, M. Cesium-containing triple cation perovskite solar cells: improved stability, reproducibility and high efficiency. *Energy Environ. Sci.* **2016**, *9*, 1989–1997.
- (7) Boonmongkolras, P.; Kim, D.; Alhabshi Esra, M.; Gereige, I.; Shin, B. Understanding effects of precursor solution aging in triple cation lead perovskite. *RSC Adv.* **2018**, *8*, 21551–21557.
- (8) Noh, J. H.; Im, S. H.; Heo, J. H.; Mandal, T. N.; Seok, S. I. Chemical Management for Colorful, Efficient, and Stable Inorganic–Organic Hybrid Nanostructured Solar Cells. *Nano Lett.* **2013**, *13*, 1764–1769.
- (9) Al-Ashouri, A.; Köhnen, E.; Li, B.; Magomedov, A.; Hempel, H.; Caprioglio, P.; Márquez, J. A.; Morales Vilches, A. B.; Kasparavicius, E.; Smith, J. A.; et al. Monolithic perovskite/silicon tandem solar cell with >29% efficiency by enhanced hole extraction. *Science* **2020**, *370*, 1300–1309.
- (10) Kim, S.; Trinh, T. T.; Park, J.; Pham, D. P.; Lee, S.; Do, H. B.; Dang, N. N.; Dao, V.-A.; Kim, J.; Yi, J. Over 30% efficiency bifacial 4-terminal perovskite-heterojunction silicon tandem solar cells with spectral albedo. *Sci. Rep.* **2021**, *11*, No. 15524.
- (11) Zhou, W.; Wen, Z.; Gao, P. Less is More: Dopant-Free Hole Transporting Materials for High-Efficiency Perovskite Solar Cells. *Adv. Energy Mater.* **2018**, *8*, No. 1702512.
- (12) Chen, B.; Rudd, P. N.; Yang, S.; Yuan, Y.; Huang, J. Imperfections and their passivation in halide perovskite solar cells. *Chem. Soc. Rev.* **2019**, *48*, 3842–3867.
- (13) Azpiroz, J. M.; Mosconi, E.; Bisquert, J.; De Angelis, F. Defect migration in methylammonium lead iodide and its role in perovskite solar cell operation. *Energy Environ. Sci.* **2015**, *8*, 2118–2127.
- (14) Senocrate, A.; Maier, J. Solid-State Ionics of Hybrid Halide Perovskites. *J. Am. Chem. Soc.* **2019**, *141*, 8382–8396.
- (15) Lopez-Varo, P.; Jiménez-Tejada, J. A.; García-Rosell, M.; Ravishankar, S.; Garcia-Belmonte, G.; Bisquert, J.; Almora, O. Device Physics of Hybrid Perovskite Solar cells: Theory and Experiment. *Adv. Energy Mater.* **2018**, *8*, No. 1702772.
- (16) Zhang, T.; Hu, C.; Yang, S. Ion Migration: A “Double-Edged Sword” for Halide-Perovskite-Based Electronic Devices. *Small Methods* **2020**, *4*, No. 1900552.
- (17) Snaith, H. J.; Abate, A.; Ball, J. M.; Eperon, G. E.; Leijtens, T.; Noel, N. K.; Stranks, S. D.; Wang, J. T.-W.; Wojciechowski, K.; Zhang, W. Anomalous Hysteresis in Perovskite Solar Cells. *J. Phys. Chem. Lett.* **2014**, *5*, 1511–1515.
- (18) Unger, E. L.; Hoke, E. T.; Bailie, C. D.; Nguyen, W. H.; Bowering, A. R.; Heumüller, T.; Christoforo, M. G.; McGehee, M. D. Hysteresis and transient behavior in current–voltage measurements of hybrid-perovskite absorber solar cells. *Energy Environ. Sci.* **2014**, *7*, 3690–3698.
- (19) Kim, H.-S.; Park, N.-G. Parameters Affecting I-V Hysteresis of CH₃NH₃PbI₃ Perovskite Solar Cells: Effects of Perovskite Crystal Size and Mesoporous TiO₂ Layer. *J. Phys. Chem. Lett.* **2014**, *5*, 2927–2934.
- (20) van Reenen, S.; Kemerink, M.; Snaith, H. J. Modeling Anomalous Hysteresis in Perovskite Solar Cells. *J. Phys. Chem. Lett.* **2015**, *6*, 3808–3814.
- (21) Kim, H.-S.; Jang, I.-H.; Ahn, N.; Choi, M.; Guerrero, A.; Bisquert, J.; Park, N.-G. Control of I-V Hysteresis in CH₃NH₃PbI₃ Perovskite Solar Cell. *J. Phys. Chem. Lett.* **2015**, *6*, 4633–4639.
- (22) Almora, O.; Aranda, C.; Zarazua, I.; Guerrero, A.; Garcia-Belmonte, G. Noncapacitive Hysteresis in Perovskite Solar Cells at Room Temperature. *ACS Energy Lett.* **2016**, *1*, 209–215.
- (23) Chen, B.; Yang, M.; Zheng, X.; Wu, C.; Li, W.; Yan, Y.; Bisquert, J.; Garcia-Belmonte, G.; Zhu, K.; Priya, S. Impact of capacitive effect and ion migration on the hysteretic behavior of perovskite solar cells. *J. Phys. Chem. Lett.* **2015**, *6*, 4693–4700.
- (24) Rong, Y. G.; Hu, Y.; Ravishankar, S.; Liu, H. W.; Hou, X. M.; Sheng, Y. S.; Mei, A. Y.; Wang, Q. F.; Li, D. Y.; Xu, M.; Bisquert, J.; Han, H. W. Tunable hysteresis effect for perovskite solar cells. *Energy Environ. Sci.* **2017**, *10*, 2383–2391.
- (25) Bisquert, J.; Guerrero, A.; Gonzales, C. Theory of Hysteresis in Halide Perovskites by Integration of the Equivalent Circuit. *ACS Phys. Chem Au* **2021**, *1*, 25–44.
- (26) Tress, W.; Baena, C.; Saliba, J. P.; Abate, M.; Graetzel, A. M. Inverted Current–Voltage Hysteresis in Mixed Perovskite Solar Cells: Polarization, Energy Barriers, and Defect Recombination. *Adv. Energy Mater.* **2016**, *6*, No. 1600396.
- (27) Akin, S. Hysteresis-Free Planar Perovskite Solar Cells with a Breakthrough Efficiency of 22% and Superior Operational Stability over 2000 h. *ACS Appl. Mater. Interfaces* **2019**, *11*, 39998–40005.
- (28) Liu, Y.; Gao, Y.; Lu, M.; Shi, Z.; Yu, W. W.; Hu, J.; Bai, X.; Zhang, Y. Ionic additive engineering for stable planar perovskite solar cells with efficiency >22%. *Chem. Eng. J.* **2021**, *426*, No. 130841.
- (29) Yoo, J. J.; Seo, G.; Chua, M. R.; Park, T. G.; Lu, Y.; Rotermund, F.; Kim, Y.-K.; Moon, C. S.; Jeon, N. J.; Correa-Baena, J.-P.; et al. J. Efficient perovskite solar cells via improved carrier management. *Nature* **2021**, *590*, 587–593.
- (30) Wang, X.; Rakstys, K.; Jack, K.; Jin, H.; Lai, J.; Li, H.; Ranasinghe, C. S. K.; Saghaei, J.; Zhang, G.; Burn, P. L.; Gentle, I. R.; Shaw, P. E. Engineering fluorinated-cation containing inverted perovskite solar cells with an efficiency of >21% and improved stability towards humidity. *Nat. Commun.* **2021**, *12*, No. 52.
- (31) Jeong, J.; Kim, M.; Seo, J.; Lu, H.; Ahlawat, P.; Mishra, A.; Yang, Y.; Hope, M. A.; Eickemeyer, F. T.; et al. Pseudo-halide anion engineering for α -FAPbI₃ perovskite solar cells. *Nature* **2021**, *592*, 381–385.
- (32) Aydin, E.; Liu, J.; Ugur, E.; Azmi, R.; Harrison, G. T.; Hou, Y.; Chen, B.; Zhumagali, S.; De Bastiani, M.; Wang, M.; et al. Ligand-bridged charge extraction and enhanced quantum efficiency enable efficient n-i-p perovskite/silicon tandem solar cells. *Energy Environ. Sci.* **2021**, *14*, 4377–4390.
- (33) Zhang, Y.; Park, N.-G. Quasi-Two-Dimensional Perovskite Solar Cells with Efficiency Exceeding 22%. *ACS Energy Lett.* **2022**, *7*, 757–765.
- (34) Gonzales, C.; Guerrero, A.; Bisquert, J. Spectral properties of the dynamic state transition in metal halide perovskite-based memristor exhibiting negative capacitance. *Appl. Phys. Lett.* **2021**, *118*, No. 073501.
- (35) Solanki, A.; Guerrero, A.; Zhang, Q.; Bisquert, J.; Sum, T. C. Interfacial Mechanism for Efficient Resistive Switching in Ruddlesden-Popper Perovskites for Non-Volatile Memories. *J. Phys. Chem. Lett.* **2020**, *11*, 463–470.
- (36) Munoz-Diaz, L.; Rosa, A. J.; Bou, A.; Sánchez, R. S.; Romero, B.; John, R. A.; Kovalenko, M. V.; Guerrero, A.; Bisquert, J. Inductive and Capacitive Hysteresis of Halide Perovskite Solar Cells and Memristors Under Illumination. *Front. Energy Res.* **2022**, *10*, No. 914115.
- (37) Xu, W.; Cho, H.; Kim, Y.-H.; Kim, Y.-T.; Wolf, C.; Park, C.-G.; Lee, T.-W. Organometal Halide Perovskite Artificial Synapses. *Adv. Mater.* **2016**, *28*, S916–S922.
- (38) Xiao, Z.; Huang, J. Energy-Efficient Hybrid Perovskite Memristors and Synaptic Devices. *Adv. Electron. Mater.* **2016**, *2*, No. 1600100.
- (39) Choi, J.; Han, J. S.; Hong, K.; Kim, S. Y.; Jang, H. W. Organic–Inorganic Hybrid Halide Perovskites for Memories, Transistors, and Artificial Synapses. *Adv. Mater.* **2018**, *30*, No. 1704002.
- (40) John, R. A.; Yantara, N.; Ng, S. E.; Patidillah, M. I. B.; Kulkarni, M. R.; Jamaludin, N. F.; Basu, J.; Ankit; Mhaisalkar, S. G.; Basu, A.; Mathews, N. Diffusive and Drift Halide Perovskite Memristive Barristors as Nociceptive and Synaptic Emulators for Neuromorphic Computing. *Adv. Mater.* **2021**, *33*, No. 2007851.

- (41) Yang, J.-Q.; Wang, R.; Wang, Z.-P.; Ma, Q.-Y.; Mao, J.-Y.; Ren, Y.; Yang, X.; Zhou, Y.; Han, S.-T. Leaky integrate-and-fire neurons based on perovskite memristor for spiking neural networks. *Nano Energy* **2020**, *74*, No. 104828.
- (42) von Hauff, E. Impedance Spectroscopy for Emerging Photovoltaics. *J. Phys. Chem. C* **2019**, *123*, 11329–11346.
- (43) Guerrero, A.; Bisquert, J.; Garcia-Belmonte, G. Impedance spectroscopy of metal halide perovskite solar cells from the perspective of equivalent circuits. *Chem. Rev.* **2021**, *121*, 14430–14484.
- (44) Guerrero, A.; Garcia-Belmonte, G.; Mora-Sero, I.; Bisquert, J.; Kang, Y. S.; Jacobsson, T. J.; Correa-Baena, J. P.; Hagfeldt, A. Properties of Contact and Bulk Impedances in Hybrid Lead Halide Perovskite Solar Cells Including Inductive Loop Elements. *J. Phys. Chem. C* **2016**, *120*, 8023–8032.
- (45) Wang, H.; Guerrero, A.; Bou, A.; Al-Mayouf, A. M.; Bisquert, J. Kinetic and material properties of interfaces governing slow response and long timescale phenomena in perovskite solar cells. *Energy Environ. Sci.* **2019**, *12*, 2054–2079.
- (46) Zohar, A.; Kedem, N.; Levine, I.; Zohar, D.; Vilan, A.; Ehre, D.; Hodes, G.; Cahen, D. Impedance Spectroscopic Indication for Solid State Electrochemical Reaction in $\text{CH}_3\text{NH}_3\text{PbI}_3$ Films. *J. Phys. Chem. Lett.* **2016**, *7*, 191–197.
- (47) Dualeh, A.; Moehl, T.; Tétreault, N.; Teuscher, J.; Gao, P.; Nazeeruddin, M. K.; Grätzel, M. Impedance spectroscopic analysis of lead iodide perovskite-sensitized solid-state solar cells. *ACS Nano* **2014**, *8*, 362–373.
- (48) Fabregat-Santiago, F.; Kulbak, M.; Zohar, A.; Vallés-Pelarda, M.; Hodes, G.; Cahen, D.; Mora-Seró, I. Deleterious Effect of Negative Capacitance on the Performance of Halide Perovskite Solar Cells. *ACS Energy Lett.* **2017**, *2*, 2007–2013.
- (49) Khan, M. T.; Huang, P.; Almohammed, A.; Kazim, S.; Ahmad, S. Mechanistic origin and unlocking of negative capacitance in perovskites solar cells. *iScience* **2021**, *24*, No. 102024.
- (50) Riquelme, A. J.; Valadez-Villalobos, K.; Boix, P. P.; Oskam, G.; Mora-Seró, I.; Anta, J. A. Understanding equivalent circuits in perovskite solar cells. Insights from drift-diffusion simulation. *Phys. Chem. Chem. Phys.* **2022**, *24*, 15657–15671.
- (51) Berruet, M.; Pérez-Martínez, J. C.; Romero, B.; Gonzales, C.; Al-Mayouf, A. M.; Guerrero, A.; Bisquert, J. Physical model for the current-voltage hysteresis and impedance of halide perovskite memristors. *ACS Energy Lett.* **2022**, *7*, 1214–1222.
- (52) Bisquert, J.; Janssen, M. From Frequency Domain to Time Transient Methods for Halide Perovskite Solar Cells: The Connections of IMPS, IMVS, TPC and TPV. *J. Phys. Chem. Lett.* **2021**, *12*, 7964–7971.
- (53) Shen, H.; Jacobs, D. A.; Wu, Y.; Duong, T.; Peng, J.; Wen, X.; Fu, X.; Karuturi, S. K.; White, T. P.; Weber, K.; Catchpole, K. R. Inverted Hysteresis in $\text{CH}_3\text{NH}_3\text{PbI}_3$ Solar Cells: Role of Stoichiometry and Band Alignment. *J. Phys. Chem. Lett.* **2017**, *8*, 2672–2680.
- (54) Wu, F.; Pathak, R.; Chen, K.; Wang, G.; Bahrami, B.; Zhang, W.-H.; Qiao, Q. Inverted Current–Voltage Hysteresis in Perovskite Solar Cells. *ACS Energy Lett.* **2018**, *3*, 2457–2460.
- (55) Nemnes, G. A.; Besleaga, C.; Stancu, V.; Dogaru, D. E.; Leonat, L. N.; Pintilie, L.; Torfason, K.; Ilkov, M.; Manolescu, A.; Pintilie, I. Normal and Inverted Hysteresis in Perovskite Solar Cells. *J. Phys. Chem. C* **2017**, *121*, 11207–11214.
- (56) Kumar, A. Numerical modelling of ion-migration caused hysteresis in perovskite solar cells. *Opt. Quantum Electron.* **2021**, *53*, 166.
- (57) Almora, O.; Lopez-Varo, P.; Cho, K. T.; Aghazada, S.; Meng, W.; Hou, Y.; Echeverría-Arrondo, C.; Zimmermann, I.; Matt, G. J.; Jiménez-Tejada, J. A.; et al. G. Ionic dipolar switching hinders charge collection in perovskite solar cells with normal and inverted hysteresis. *Sol. Energy Mater. Sol. Cells* **2019**, *195*, 291–298.
- (58) Xiang, J.; Li, Y.; Huang, F.; Zhong, D. Effect of interfacial recombination, bulk recombination and carrier mobility on the J–V hysteresis behaviors of perovskite solar cells: a drift-diffusion simulation study. *Phys. Chem. Chem. Phys.* **2019**, *21*, 17836–17845.
- (59) Neukom, M. T.; Züfle, S.; Knapp, E.; Makha, M.; Hany, R.; Ruhstaller, B. Why perovskite solar cells with high efficiency show small IV-curve hysteresis. *Sol. Energy Mater. Sol. Cells* **2017**, *169*, 159–166.
- (60) Neukom, M. T.; Schiller, A.; Züfle, S.; Knapp, E.; Ávila, J.; Pérez-del-Rey, D.; Dreesen, C.; Zanoni, K. P. S.; Sessolo, M.; Bolink, H. J.; Ruhstaller, B. Consistent Device Simulation Model Describing Perovskite Solar Cells in Steady-State, Transient, and Frequency Domain. *ACS Appl. Mater. Interfaces* **2019**, *11*, 23320–23328.
- (61) Richardson, G.; O’Kane, S. E. J.; Niemann, R. G.; Peltola, T. A.; Foster, J. M.; Cameron, P. J.; Walker, A. B. Can slow-moving ions explain hysteresis in the current-voltage curves of perovskite solar cells? *Energy Environ. Sci.* **2016**, *9*, 1476–1485.
- (62) Yeow, Q. J.; Cuhadar, C.; Tay, W. K.; Tan, E. L. J.; Johnson, K.; Whang, S. E.; Tsao, H. N. Converting Solar Cells to Photocapacitors without the Incorporation of Additional Capacitive Components. *ACS Appl. Energy Mater.* **2022**, *5*, 6746–6753.
- (63) Hodgkin, A. L.; Huxley, A. F. A quantitative description of membrane current and its application to conduction and excitation in nerve. *J. Physiol.* **1952**, *117*, 500–544.
- (64) Izhikevich, E. M. *Dynamical Systems in Neuroscience*, MIT Press, 2007.
- (65) Gerstner, W.; Kistler, W. M.; Naud, R.; Paninski, L. *Neuronal Dynamics. From Single Neurons to networks and Models of Cognition*, Cambridge University Press, 2014.
- (66) Bisquert, J. A frequency domain analysis of excitability and bifurcations of Fitzhugh-Nagumo neuron model. *J. Phys. Chem. Lett.* **2021**, *12*, 11005–11013.
- (67) Bisquert, J. Hopf bifurcations in electrochemical, neuronal, and semiconductor systems analysis by impedance spectroscopy. *Appl. Phys. Rev.* **2022**, *9*, No. 011318.
- (68) Bisquert, J.; Guerrero, A. Dynamic Instability and Time Domain Response of a Model Halide Perovskite Memristor for Artificial Neurons. *J. Phys. Chem. Lett.* **2022**, *13*, 3789–3795.
- (69) Aranda, C.; Guerrero, A.; Bisquert, J. Ionic Effect Enhances Light Emission and the Photovoltage of Methylammonium Lead Bromide Perovskite Solar Cells by Reduced Surface Recombination. *ACS Energy Lett.* **2019**, *4*, 741–746.
- (70) Zimmermann, E.; Ehrenreich, P.; Pfadler, T.; Dorman, J. A.; Weickert, J.; Schmidt-Mende, L. Erroneous efficiency reports harm organic solar cell research. *Nat. Photonics* **2014**, *8*, 669–672.
- (71) Christians, J. A.; Manser, J. S.; Kamat, P. V. Best Practices in Perovskite Solar Cell Efficiency Measurements. Avoiding the Error of Making Bad Cells Look Good. *J. Phys. Chem. Lett.* **2015**, *6*, 852–857.
- (72) Wang, Y.; Liu, X.; Zhou, Z.; Ru, P.; Chen, H.; Yang, X.; Han, L. Reliable Measurement of Perovskite Solar Cells. *Adv. Mater.* **2019**, *31*, No. 1803231.
- (73) Wu, F.; Pathak, R.; Qiao, Q. Origin and alleviation of J–V hysteresis in perovskite solar cells: A short review. *Catal. Today* **2021**, *374*, 86–101.
- (74) Correa-Baena, J.-P.; Turren-Cruz, S.-H.; Tress, W.; Hagfeldt, A.; Aranda, C.; Shooshtari, L.; Bisquert, J.; Guerrero, A. Changes from Bulk to Surface Recombination Mechanisms between Pristine and Cycled Perovskite Solar Cells. *ACS Energy Lett.* **2017**, *2*, 681–688.
- (75) Belisle, R. A.; Nguyen, W. H.; Bowring, A. R.; Calado, P.; Li, X.; Irvine, S. J. C.; McGehee, M. D.; Barnes, P. R. F.; O’Regan, B. C. Interpretation of inverted photocurrent transients in organic lead halide perovskite solar cells: proof of the field screening by mobile ions and determination of the space charge layer widths. *Energy Environ. Sci.* **2017**, *10*, 192–204.
- (76) Pockett, A.; Spence, M.; Thomas, S. K.; Raptis, D.; Watson, T.; Carmie, M. J. Beyond the First Quadrant: Origin of the High Frequency Intensity-Modulated Photocurrent/Photovoltage Spectroscopy Response of Perovskite Solar Cells. *Sol. RRL* **2021**, *5*, No. 2100159.
- (77) Ravishankar, S.; Almora, O.; Echeverría-Arrondo, C.; Ghahremanirad, E.; Aranda, C.; Guerrero, A.; Fabregat-Santiago, F.; Zaban, A.; Garcia-Belmonte, G.; Bisquert, J. Surface Polarization Model for the Dynamic Hysteresis of Perovskite Solar Cells. *J. Phys. Chem. Lett.* **2017**, *8*, 915–921.

- (78) Almora, O.; Zarazua, I.; Mas-Marza, E.; Mora-Sero, I.; Bisquert, J.; Garcia-Belmonte, G. Capacitive dark currents, hysteresis, and electrode polarization in lead halide perovskite solar cells. *J. Phys. Chem. Lett.* **2015**, *6*, 1645–1652.
- (79) Hernández-Balaguera, E.; del Pozo, G.; Arredondo, B.; Romero, B.; Pereyra, C.; Xie, H.; Lira-Cantú, M. Unraveling the Key Relationship Between Perovskite Capacitive Memory, Long Timescale Cooperative Relaxation Phenomena, and Anomalous J–V Hysteresis. *Sol. RRL* **2021**, *5*, No. 2000707.
- (80) Contreras, L.; Idígoras, J.; Todinova, A.; Salado, M.; Kazim, S.; Ahmad, S.; Anta, J. A. Specific cation interactions as the cause of slow dynamics and hysteresis in dye and perovskite solar cells: a small-perturbation study. *Phys. Chem. Chem. Phys.* **2016**, *18*, 31033–31042.
- (81) Sarker, S.; Seo, H. W.; Jin, Y.-K.; Lee, K.-S.; Lee, M.; Kim, D. M. On the Hysteresis of Current Density–Voltage Curves of Dye-sensitized Solar Cells. *Electrochim. Acta* **2015**, *182*, 493–499.
- (82) Courtier, N. E. Interpreting Ideality Factors for Planar Perovskite Solar Cells: Ectypal Diode Theory for Steady-State Operation. *Phys. Rev. Appl.* **2020**, *14*, No. 024031.
- (83) Almora, O.; Cho, K. T.; Aghazada, S.; Zimmermann, I.; Matt, G. J.; Brabec, C. J.; Nazeeruddin, M. K.; Garcia-Belmonte, G. Discerning recombination mechanisms and ideality factors through impedance analysis of high-efficiency perovskite solar cells. *Nano Energy* **2018**, *48*, 63–72.
- (84) Tress, W.; Yavari, M.; Domanski, K.; Yadav, P.; Niesen, B.; Correa Baena, J. P.; Hagfeldt, A.; Graetzel, M. Interpretation and evolution of open-circuit voltage, recombination, ideality factor and subgap defect states during reversible light-soaking and irreversible degradation of perovskite solar cells. *Energy Environ. Sci.* **2018**, *11*, 151–165.
- (85) Mora-Seró, I.; Bisquert, J.; Fabregat-Santiago, F.; Garcia-Belmonte, G.; Zoppi, G.; Durose, K.; Proskuryakov, Y. Y.; Oja, I.; Belaidi, A.; Dittrich, T.; et al. Implications of the negative capacitance observed at forward bias in nanocomposite and polycrystalline solar cells. *Nano Lett.* **2006**, *6*, 640–650.
- (86) Bisquert, J. Chemical capacitance of nanostructured semiconductors: its origin and significance for heterogeneous solar cells. *Phys. Chem. Chem. Phys.* **2003**, *5*, 5360–5364.
- (87) Guerrero, A.; Garcia-Belmonte, G.; Mora-Sero, I.; Bisquert, J.; Kang, Y. S.; Jacobsson, T. J.; Correa-Baena, J.-P.; Hagfeldt, A. Properties of Contact and Bulk Impedances in Hybrid Lead Halide Perovskite Solar Cells Including Inductive Loop Elements. *J. Phys. Chem. C* **2016**, *120*, 8023–8032.
- (88) Wang, H.; Guerrero, A.; Bou, A.; Al-Mayouf, A. M.; Bisquert, J. Kinetic and material properties of interfaces governing slow response and long timescale phenomena in perovskite solar cells. *Energy Environ. Sci.* **2019**, *12*, 2054–2079.
- (89) Zarazua, I.; Han, G.; Boix, P. P.; Mhaisalkar, S.; Fabregat-Santiago, F.; Mora-Seró, I.; Bisquert, J.; Garcia-Belmonte, G. Surface Recombination and Collection Efficiency in Perovskite Solar Cells from Impedance Analysis. *J. Phys. Chem. Lett.* **2016**, *7*, 5105–5113.
- (90) Caprioglio, P.; Stolterfoht, M.; Wolff, C. M.; Unold, T.; Rech, B.; Albrecht, S.; Neher, D. On the Relation between the Open-Circuit Voltage and Quasi-Fermi Level Splitting in Efficient Perovskite Solar Cells. *Adv. Energy Mater.* **2019**, *9*, No. 1901631.
- (91) Almora, O.; Garcia-Belmonte, G. Light capacitances in silicon and perovskite solar cells. *Sol. Energy* **2019**, *189*, 103–110.
- (92) Pockett, A.; Eperon, G. E.; Sakai, N.; Snaith, H. J.; Peter, L. M.; Cameron, P. J. Microseconds, milliseconds and seconds: deconvoluting the dynamic behaviour of planar perovskite solar cells. *Phys. Chem. Chem. Phys.* **2017**, *19*, 5959–5970.
- (93) Garcia-Belmonte, G.; Bisquert, J. Distinction between Capacitive and Noncapacitive Hysteretic Currents in Operation and Degradation of Perovskite Solar Cells. *ACS Energy Lett.* **2016**, *1*, 683–688.
- (94) Bisquert, J.; Guerrero, A. Chemical Inductor. *J. Am. Chem. Soc.* **2022**, *144*, 5996–6009.
- (95) Alvarez, A. O.; Arcas, R.; Aranda, C. A.; Bethencourt, L.; Mas-Marzá, E.; Saliba, M.; Fabregat-Santiago, F. Negative Capacitance and Inverted Hysteresis: Matching Features in Perovskite Solar Cells. *J. Phys. Chem. Lett.* **2020**, *11*, 8417–8423.
- (96) Bou, A.; Pockett, A.; Raptis, D.; Watson, T.; Carnie, M. J.; Bisquert, J. Beyond Impedance Spectroscopy of Perovskite Solar Cells: Insights from the Spectral Correlation of the Electrooptical Frequency Techniques. *J. Phys. Chem. Lett.* **2020**, *11*, 8654–8659.
- (97) Jacobs, D. A.; Shen, H.; Pfeffer, F.; Peng, J.; White, T. P.; Beck, F. J.; Catchpole, K. R. The Two Faces of Capacitance: New Interpretations for Electrical Impedance Measurements of Perovskite Solar Cells and their Relation to Hysteresis. *J. Appl. Phys.* **2018**, *124*, No. 225702.
- (98) Moia, D.; Gelmetti, I.; Calado, P.; Fisher, W.; Stringer, M.; Game, O.; Hu, Y.; Docampo, P.; Lidzey, D.; Palomares, E.; Nelson, J.; Barnes, P. R. F. Ionic-to-electronic current amplification in hybrid perovskite solar cells: ionically gated transistor-interface circuit model explains hysteresis and impedance of mixed conducting devices. *Energy Environ. Sci.* **2019**, *12*, 1296–1308.
- (99) Ebadi, F.; Taghavinia, N.; Mohammadpour, R.; Hagfeldt, A.; Tress, W. Origin of Apparent Light-Enhanced and Negative Capacitance in Perovskite Solar Cells. *Nat. Commun.* **2019**, *10*, No. 1574.
- (100) Choi, W.; Song, S. W.; Han, S. G.; Cho, K. The Origin of Photoinduced Capacitance in Perovskite Solar Cells: Beyond Ionic-to-Electronic Current Amplification. *Adv. Electron. Mater.* **2020**, *6*, No. 2000030.
- (101) Klotz, D. Negative capacitance or inductive loop? – A general assessment of a common low frequency impedance feature. *Electrochem. Commun.* **2019**, *98*, 58–62.
- (102) Hernández-Balaguera, E.; Bisquert, J. Negative Transient Spikes in Halide Perovskites. *ACS Energy Lett.* **2022**, 2602–2610.
- (103) Ghahremanirad, E.; Bou, A.; Olyae, S.; Bisquert, J. Inductive Loop in the Impedance Response of Perovskite Solar Cells Explained by Surface Polarization Model. *J. Phys. Chem. Lett.* **2017**, *8*, 1402–1406.
- (104) Pockett, A.; Carnie, M. J. Ionic Influences on Recombination in Perovskite Solar Cells. *ACS Energy Lett.* **2017**, *2*, 1683–1689.
- (105) Kumar, R.; Kumar, J.; Srivastava, P.; Moghe, D.; Kabra, D.; Bag, M. Unveiling the Morphology Effect on the Negative Capacitance and Large Ideality Factor in Perovskite Light-Emitting Diodes. *ACS Appl. Mater. Interfaces* **2020**, *12*, 34265–34273.
- (106) Moia, D.; Gelmetti, I.; Calado, P.; Fisher, W.; Stringer, M.; Game, O.; Hu, Y.; Docampo, P.; Lidzey, D.; Palomares, E.; et al. Ionic-to-electronic current amplification in hybrid perovskite solar cells: ionically gated transistor-interface circuit model explains hysteresis and impedance of mixed conducting devices. *Energy Environ. Sci.* **2019**, *12*, 1296–1308.
- (107) Kovalenko, A.; Pospisil, J.; Krajcovic, J.; Weiter, M.; Guerrero, A.; Garcia-Belmonte, G. Interface inductive currents and carrier injection in hybrid perovskite single crystals. *Appl. Phys. Lett.* **2017**, *111*, No. 163504.
- (108) Jacobs, D. A.; Shen, H.; Pfeffer, F.; Peng, J.; White, T. P.; Beck, F. J.; Catchpole, K. R. The two faces of capacitance: New interpretations for electrical impedance measurements of perovskite solar cells and their relation to hysteresis. *J. Appl. Phys.* **2018**, *124*, No. 225702.
- (109) Ebadi, F.; Taghavinia, N.; Mohammadpour, R.; Hagfeldt, A.; Tress, W. Origin of apparent light-enhanced and negative capacitance in perovskite solar cells. *Nat. Commun.* **2019**, *10*, No. 1574.
- (110) Tong, C.-J.; Cai, X.; Zhu, A.-Y.; Liu, L.-M.; Prezhdo, O. V. How Hole Injection Accelerates Both Ion Migration and Nonradiative Recombination in Metal Halide Perovskites. *J. Am. Chem. Soc.* **2022**, *144*, 6604–6612.
- (111) Dhifaoui, H.; Hemasiri, N. H.; Aloui, W.; Bouazizi, A.; Kazim, S.; Ahmad, S. An Approach to Quantify the Negative Capacitance Features in a Triple-Cation based Perovskite Solar Cells. *Adv. Mater. Interfaces* **2021**, *8*, No. 2101002.
- (112) Zhu, H.; Pan, L.; Eickemeyer, F. T.; Hope, M. A.; Ouellette, O.; Alanazi, A. Q. M.; Gao, J.; Baumeler, T. P.; Li, X.; Wang, S.; et al. M. Efficient and Stable Large Bandgap MAPbBr₃ Perovskite Solar Cell

Attaining an Open Circuit Voltage of 1.65 V. *ACS Energy Lett.* **2022**, *7*, 1112–1119.

(113) Wu, C.-G.; Chiang, C.-H.; Chang, S. H. A perovskite cell with a record-high-Voc of 1.61 V based on solvent annealed CH₃NH₃PbBr₃/ICBA active layer. *Nanoscale* **2016**, *8*, 4077–4085.

(114) Bisquert, J. *The Physics of Solar Energy Conversion*; CRC Press: Boca Raton, 2020.

Recommended by ACS

Direct Measurements of Interfacial Photovoltage and Band Alignment in Perovskite Solar Cells Using Hard X-ray Photoelectron Spectroscopy

Sebastian Svanström, Ute B. Cappel, *et al.*

FEBRUARY 27, 2023

ACS APPLIED MATERIALS & INTERFACES

READ 

Direct Tracking of Charge Carrier Drift and Extraction from Perovskite Solar Cells by Means of Transient Electroabsorption Spectroscopy

Vidmantas Jašinskas, Vidmantas Gulbinas, *et al.*

JANUARY 11, 2023

ACS APPLIED ELECTRONIC MATERIALS

READ 

Degradation Analysis of Triple-Cation Perovskite Solar Cells by Electrochemical Impedance Spectroscopy

Jeevan Torres, Antonio Abate, *et al.*

OCTOBER 07, 2022

ACS APPLIED ENERGY MATERIALS

READ 

Degradation of Perovskite Photovoltaics Manifested in the Cross-Sectional Potential Profile Studied by Quantitative Kelvin Probe Force Microscopy

Maki Hiraoka, Yasuhiro Shirai, *et al.*

APRIL 08, 2022

ACS APPLIED ENERGY MATERIALS

READ 

Get More Suggestions >